

1 **Intense interface seismicity triggered by a shallow slow-slip event**
2 **in the Central-Ecuador subduction zone**

3

4 Martin Vallée ^{1,*}, Jean-Mathieu Nocquet ¹, Jean Battaglia ², Yvonne Font ¹, Monica Segovia ³,
5 Marc Régnier ¹, Patricia Mothes ³, Paul Jarrin ³, David Cisneros ⁴, Sandro Vaca ³, Hugo
6 Yepes ³, Xavier Martin ¹, Nicole Béthoux ¹, and Mohamed Chlieh ¹

7

8

9 ¹ Geoazur, Université de Nice Sophia-Antipolis, IRD-CNRS-OCA, Nice, France.

10

11 ² Laboratoire Magmas et Volcans, Université Blaise Pascal-CNRS-IRD, Clermont-
12 Ferrand, France.

13

14 ³ IG-EPN, Instituto Geofísico, Escuela Politécnica Nacional, Quito, Ecuador.

15

16 ⁴ IGM-EC, Military Geographic Institute of Ecuador.

17

18 * Now at : Institut de Physique du Globe de Paris, Sorbonne Paris Cité, Univ Paris

19 Diderot, UMR 7154 CNRS, Paris, France

20

21

22

23

24

25

26

Abstract

27 We document a one week long slow-slip event (SSE) with an equivalent moment
28 magnitude of 6.0-6.3 which occurred in August 2010 below La Plata Island (Ecuador), south
29 of the rupture area of the Mw=8.8 1906 megathrust earthquake. GPS data reveal that the SSE
30 occurred at a depth of about 10km, within the downdip part of a shallow (<15km), isolated,
31 locked patch along the subduction interface. The availability of both broad-band seismometer
32 and continuous geodetic station located at the La Plata Island, 10km above the SSE, enables a
33 careful analysis of the relationships between slow and rapid processes of stress release along
34 the subduction interface. During the slow slip sequence, the seismic data shows a sharp
35 increase of the local seismicity, with more than 650 earthquakes detected, among which 50
36 have a moment magnitude between 1.8 and 4.1. However, the cumulative moment released
37 through earthquakes accounts at most for 0.2% of the total moment release estimated from
38 GPS displacements. Most of the largest earthquakes are located along or very close to the
39 subduction interface with focal mechanism consistent with the relative plate motion. While
40 the earthquake sizes show a classical distribution (Gutenberg-Richter law with a b-value close
41 to 1), the space-time occurrence presents a specific pattern. First, the largest earthquakes
42 appear to occur randomly during the slow slip sequence, which further evidence that the
43 seismicity is driven by the stress fluctuations related to aseismic slip. Moreover, the seismicity
44 observed during the SSE consists in individual events and families of repeating earthquakes.
45 These observations indicate that the stress increment induced by the episodic aseismic slip
46 may lead both to sudden seismic moment release and to progressive rupture within small
47 locked patches. This study offers an *a posteriori* interpretation of the seismogenesis in the
48 Central-Ecuador subduction zone, where intense seismic swarms have been regularly
49 observed (1977, 1998, 2002, 2005). These swarms have likely been triggered by large
50 magnitude slow-slip events.

51 **1) Introduction**

52

53 Slow slip events (SSE) have been documented in numerous segments of the Circum
54 Pacific subduction zone (Cascades, Japan, Mexico, Costa Rica, see *Schwartz and Rokosky,*
55 2007 for a review). These SSEs, which can last from days to months, occur along the
56 subduction interface with a mechanism releasing some of the stress accumulated by plate
57 convergence. First observed at depths of 30-50km, close to the downdip limit of strongly
58 coupled subduction interfaces (Southwest Japan, *Hirose et al., 1999*; Cascades, *Dragert et al.,*
59 2001), they were interpreted as the expression of the brittle-ductile transition zone located at
60 the downdip limit of the seismogenic zone. Above this zone and up to shallow depths, the
61 interface accumulates slip deficit, which is mostly released during large megathrust
62 earthquakes. Below it, the plates are freely slipping. More recently, SSEs were also observed
63 at shallower depths, at least in three subduction zones (Boso Peninsula, Japan, *Ozawa et al.,*
64 2003, *Sagiya, 2004*; Hikurangi, New Zealand, *Douglas et al., 2005, McCaffrey et al., 2008,*
65 *Wallace and Beavan, 2010*; Nicoya, Costa Rica, *Outerbridge et al., 2010*). Nonetheless, in the
66 two latter cases (Hikurangi, northern New Zealand and Costa Rica), the locus of the SSEs is
67 consistent with the view of a downdip brittle-ductile transition zone, as the locking depth is
68 shallow in these two areas. The case of the Boso peninsula shows a more complex pattern,
69 because the location of the 1996 SSE appears to be adjacent to a coupled zone (*Sagiya, 2004*).

70

71 Since the discovery of SSEs, this proximity between the slow slip processes and
72 earthquake-prone areas has raised the question of their seismic triggering potential (e.g.
73 *Dragert et al., 2001; Mazzotti and Adams, 2004*). As a matter of fact, although SSEs should
74 inhibit the seismic rupture where they occur, the stress increment they induce may promote
75 the seismic rupture in the surrounding fault segments when near to failure. The close

76 relationships between SSEs and seismic processes have been evidenced, but usually not with
77 classical seismicity: SSEs are often shown to be accompanied by a peculiar seismic activity,
78 referred as non-volcanic tremors (NVT, *Rogers and Dragert, 2003*). These NVTs clearly
79 differ from the usual seismicity because of their long duration and absence of clear wave
80 arrivals. So far, triggering of large interplate earthquakes by slow slip events has not been
81 observed, although aseismic slip has been proposed to precede the 2011 Tohoku (Japan)
82 earthquake, (*Kato et al., 2012*). Concerning the lower magnitude seismicity, earthquakes rate
83 has been shown to clearly increase during the SSEs in only two subduction areas, namely the
84 Boso peninsula (*Ozawa et al., 2003; Sagiya, 2004*), and the Hikurangi subduction zone
85 (*Delahaye et al., 2009*). In the case of the Guerrero SSEs (Mexico), *Liu et al. (2007)* have
86 identified some changes of the seismicity pattern, but they were clearer at the beginning and
87 end of the SSEs than during the process itself. An observation shared by these SSEs is that
88 direct seismic triggering appears to be mainly restricted to shallow SSEs (*Delahaye et al.,*
89 *2009*), even if a recent study (*Vidale et al., 2011*) also points out the triggering of a few
90 earthquakes during a 2010 SSE in the Cascades region. In the case of the Hikurangi
91 subduction zone, *Delahaye et al. (2009)* have shown some properties of this associated
92 seismicity. In particular, they show that seismicity is consistent with reverse faulting downdip
93 of the SSE, on or close to the subduction interface.

94
95 In this study, we first introduce some characteristics of the Central Ecuador subduction
96 zone (see Figure 1) in terms of seismicity and coupling derived from GPS, and show that
97 Central Ecuador shares some common characteristics with the Northern Hikurangi (New
98 Zealand) subduction zone. More specifically, the interseismic interplate coupling is restricted
99 to the shallower part of the interface located between the trench and La Plata island. In this
100 context, a shallow SSE occurred during one week, in August 2010, within the lower part of

101 the coupled interface. The geometry of observation is unusual and favorable, as we benefit
102 from a GPS and seismic station located on the La Plata Island (Figure 1), only 35 km from the
103 trench and, as will be shown, directly above the 10km-deep slow slip area. Seismic data
104 reveal a strong and abrupt change of the microseismicity during the SSE. We describe how
105 this seismicity is organized - in terms of location, time and mechanisms - and how it is
106 intimately related to the slow slip itself. This study confirms and further documents the
107 seismic triggering potential of SSEs, even if it is restricted in this particular case to small
108 earthquakes. Moreover, the swarm nature of the seismic crisis, together with the frequent past
109 occurrence of large swarms in this area, indicate that slow slip processes plays an important
110 role in the stress release along this segment of the Nazca/south America subduction zone.

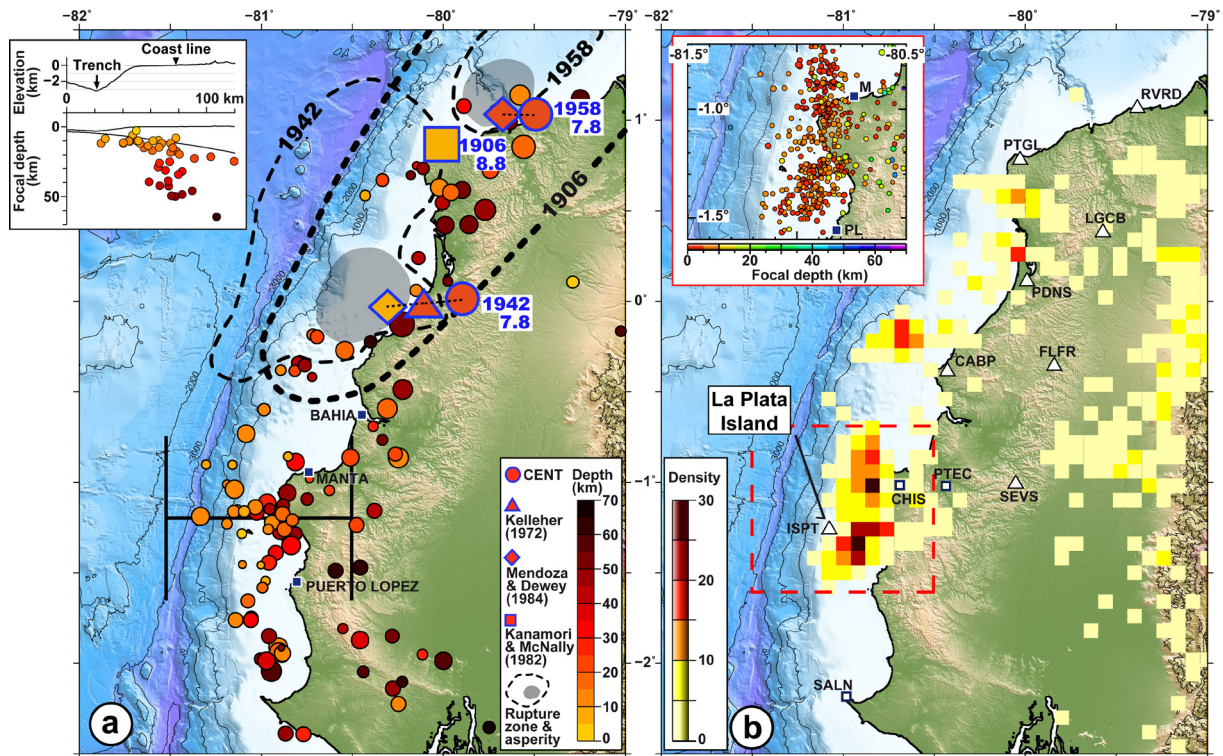
111

112 **2) Seismicity and interseismic coupling along the Central Ecuador**

113 **subduction zone**

114

115 The central Ecuador margin is a peculiar region of the North-Andean subduction zone.
116 While mega-thrust earthquakes (moment magnitude larger than 7.7) have been observed
117 North of the latitude $\sim 0.5^{\circ}\text{S}$ in 1906, 1942, 1958, 1979 (Figure 1), they seem to be absent in
118 Southern Ecuador and Northern Peru (*Dorbath et al.*, 1990; *Bilek*, 2010). Seismically, the
119 region located at latitude $\sim 1^{\circ}\text{S}$ (offshore Bahia and Manta) thus appears to be a transitional
120 area, delimiting the termination of the major earthquakes activity. However, this simple
121 observation is reversed if looking at the moderate to strong (up to magnitude 6.5) earthquakes,
122 detected by the global networks since 1960 (Figure 1a, *Manchuel et al.*, 2011): for this range
123 of magnitudes, the seismic activity is higher around 1°S than in Northern Ecuador.



124
 125 *Figure 1 : Seismicity of the Ecuadorian subduction zone. a) Map of earthquake epicenters and*
 126 *rupture area of major earthquakes. Black-contoured circles are earthquakes from the EHB*
 127 *catalog (Engdahl et al., 1998) for the 1960-2007 period. Depth is indicated by the color scale,*
 128 *and the symbol size is relative to Mb magnitudes, ranging from to 3.8 to 6.5. The epicenters of*
 129 *historical earthquakes compiled from several studies are blue contoured (CENT catalog is*
 130 *from Engdahl and Villaseñor, 2002). Rupture zones and asperity locations are from Beck and*
 131 *Ruff (1984) and Swenson and Beck (1996). The inset shows the East-West cross-section*
 132 *(location and width are marked on the map), with black lines representing topography and top*
 133 *of the subducting Nazca Plate (modified after Graindorge et al., 2004). b) Earthquake density*
 134 *map from a relocation work (Font et al., 2013) of the local network catalogue (1994-2007, IG-*
 135 *EPN). Cells including only one earthquake are not shown. Relocated earthquakes within the*
 136 *red dashed box are shown in the upper left inset. The continuous stations (seismometer and*
 137 *GPS) of the ADN project (installed in 2008-2009) are shown by triangles. Two permanent GPS*
 138 *stations of the IG-EPN (CHIS and SALN) and one (PTEC) from the Militar Geographic*

139 *Institute (IGM) are shown by squares. In both subfigures, bathymetry is contoured and labeled*
140 *(in m).*

141 This observation is further confirmed by the characteristics of the local seismicity. We
142 make use of the 1994-2007 local catalog (RENSIG) provided by the Institute of Geophysics
143 of Quito (IG-EPN). Earthquakes of this catalog have been relocated using the MAXI
144 technique (Font *et al.*, 2004; Theunissen *et al.*, 2012), an *a priori* 3D velocity model and a
145 selection of seismic stations (Font *et al.*, 2013), resulting in the MAXI-3D catalog. The *a*
146 *priori* 3D velocity model is constructed from the integration of independent geophysical and
147 geological data (see Font *et al.*, 2013 for references). The regional model represents the upper
148 crust and mantle intricacies of the subduction zone and associated velocity gradients such as:
149 the surface topography variations (from the oceanic trench to the volcanic arc), the
150 compositional difference between the oceanic subducting plate and the oceanic/continental
151 overriding plate, the lateral seismic velocity variations produced by local tectonic structures
152 (such as the subducting Carnegie ridge, the forearc sedimentary basins or the backarc basins),
153 the crustal thickness and Moho discontinuity. Close to La Plata Island (Figure 1), the
154 knowledge of crustal structure benefits from marine geophysical surveys (Graindorge *et al.*,
155 2004) and local seismicity analyses (Béthoux *et al.*, 2011). Quality criteria, related to the
156 station distribution, reduce the number of earthquakes of the MAXI-3D catalog compared to
157 the RENSIG catalog (by about 50% in the offshore domain). The earthquake density map
158 shown in Figure 1b counts the number of earthquakes in cells of 0.09°x 0.09°. The intense
159 seismic activity, offshore the Manta Peninsula and close to La Plata Island, appears even more
160 clearly than in the EHB catalog (Engdahl *et al.*, 1998) map of Figure 1a.

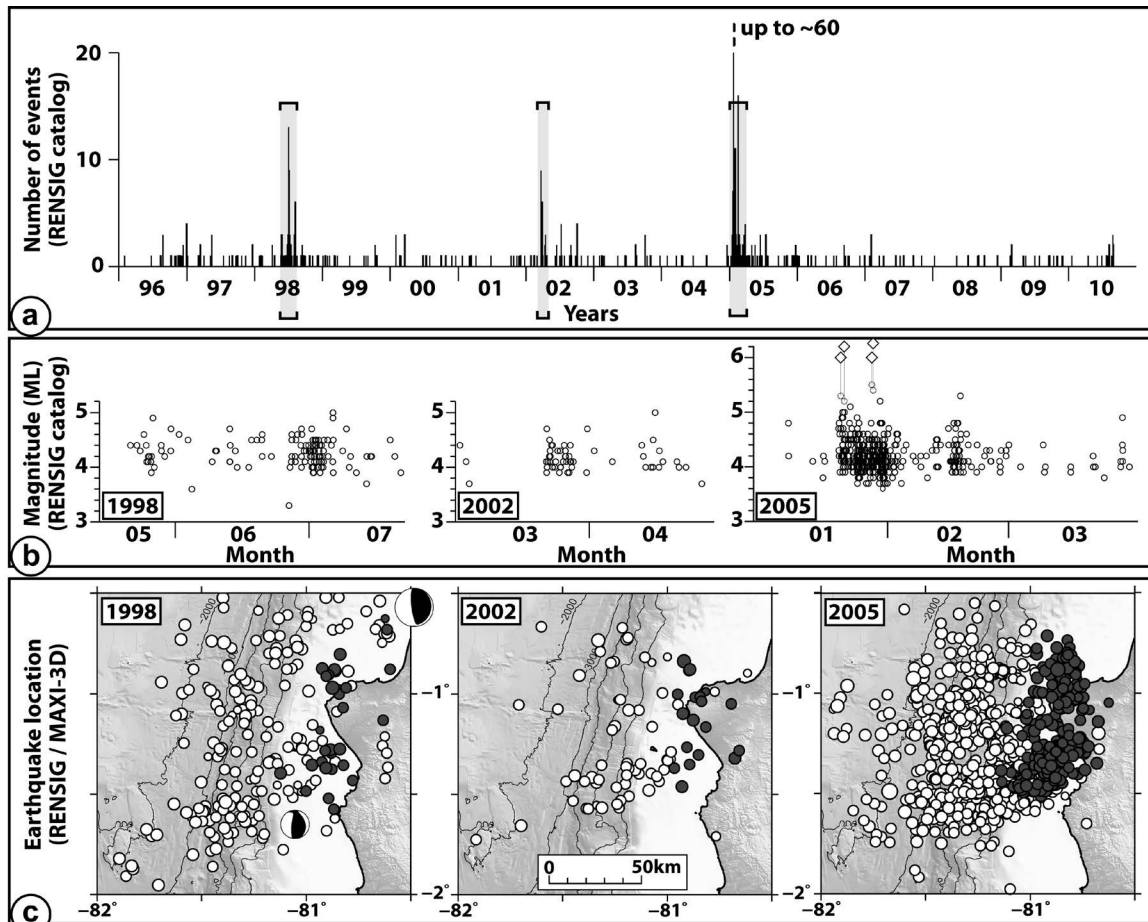
161

162 In the La Plata – Manta region, the abundant seismicity is mostly due to repeated
163 activity, clustered in space and time. In space, this seismicity extends parallel to the trench,

164 covering a 80 km long and 30 km wide area (from MAXI-3D catalog). In depth, the
165 hypocenters are distributed from the interplate contact zone (from *Graindorge et al.*, 2004) up
166 to the surface (see Figure 8, in *Font et al.*, 2013). Focal mechanisms of the largest earthquakes
167 of the 1998 and 2005 sequence (from Global CMT, Ekström et al., 2012) exhibit thrust
168 motion (Figure 2). From the hypocenter locations and the associated inverse motion, we infer
169 that past clusters occurred on or close to the subduction interface. In time, these clusters
170 occurred in 1998 (*Segovia*, 2001), 2002 and 2005 (*Segovia*, 2009; *Vaca et al.*, 2009), and
171 lasted from one to three months (Figure 2). We define these three periods as earthquake
172 swarms as they match the criteria proposed by *Holtkamp and Brudzinski* (2011): the
173 seismicity rate increase is not related to a clear triggering main shock, several earthquakes
174 have a magnitude close to the largest earthquake of the cluster, and the activity of the cluster
175 terminates abruptly. The 2005 episode was the largest of these swarms, with 485 events with
176 magnitude ML larger than 4, among which four main shocks have a moment magnitude
177 between 6 and 6.2 (Figure 2, *Vaca et al.*, 2009). The 2005 seismic swarm has also been
178 detected at the global scale, as 43 earthquakes were located by the NEIC (with a magnitude
179 threshold of 4-4.5) in January-February 2005 (*Holtkamp and Brudzinski*, 2011; *Holtkamp et*
180 *al.*, 2011). In this area, these last two studies also point out a smaller swarm in 1977.

181

182



183

184 *Figure 2: Earthquake occurrence characteristics in the La Plata – Manta region*

185 *(corresponding to the dashed red box in Figure 1b). a) Histogram of earthquake occurrence*

186 *(RENSIG catalog) from 1996 to 2010 (bin is 1 day). b) Earthquake magnitude versus time for*

187 *the 3 main periods of activity. ML is represented by circles (from RENSIG) and Mw by*

188 *diamonds (Vaca et al., 2009). c) Epicentral locations (RENSIG) of earthquakes presented in*

189 *b) are shown by white circles. Relocations in a 3D model (MAXI-3D catalog; Theunissen et*

190 *al., 2012; Font et al., 2013) are shown by grey circles. Focal mechanisms of earthquakes with*

191 *magnitude above ~5.5 are from Global CMT (Ekström et al., 2012).*

192

193 Since the end of 2008, the Ecuadorian coast is continuously monitored by an array of 9

194 stations including on each site a GPS equipment (recording at 5Hz), a broad-band

195 seismometer, and an accelerometer (Andes Du Nord “ADN” project, Figure 1). This French-

196 Ecuadorian project has been built in collaboration with the IG-EPN and the French laboratory
197 of Geoazur. The new instrumentation, together with the stations of the IG-EPN seismic and
198 GPS networks, allow us to monitor a broad range of processes acting in a subduction zone,
199 including tectonic deformation, aseismic movements or large earthquakes. During the last
200 three years, it has also helped to better image the interseismic coupling along the subduction
201 interface. To determine its spatial distribution, we have used a combination of the continuous
202 GPS stations progressively installed since 2008 and campaign data observed since 1994. The
203 full description of the processing strategy will be described in a separate manuscript (*Nocquet*
204 *et al.*, in preparation), but we discuss here the relevant points for the analysis of the SSE and
205 interseismic models. A further analysis of the interseismic coupling along the Ecuadorian
206 subduction zone will also be described in a separate study (*Chlieh et al.* in preparation). For
207 the purpose of this study, we focus here on the interseismic coupling around the segment of
208 La Plata Island before the 2010 SSE.

209

210 When expressed in a stable South America reference frame, velocities in southern
211 Ecuador show the contribution of crustal tectonics and elastic deformation induced by the
212 interseismic locking along part of the subduction interface. In order to separate the two
213 contributions, we take advantage of low coupling observed in southern Ecuador (around
214 latitude 2°S) where GPS sites behave rigidly at the millimeter per year level. In particular, no
215 shortening in the East-West direction is detected and the velocities are consistent with the
216 ones observed in southern Colombia (IGS site BOGT). Such a motion represents the motion
217 of the North Andean Block (NAB) as introduced by previous studies (*Pennington*, 1981,
218 *Gutscher et al.*, 1999, *Trenkamp et al.*, 2002, *White et al.*, 2003). It is equivalent to a constant
219 translation motion of 9.5mm/yr in a N75-80° direction for southern Ecuador (*Nocquet et al.*,
220 in preparation) which is about twice faster and more eastward oriented than what was

221 previously proposed. Residual velocities with respect to the North Andean Block, presented in
222 Figure 3, are then inverted to determine the elastic locking along the subduction interface.

223

224 We use the back-slip approach introduced by *Savage* (1983) to invert for the interplate
225 coupling along the subduction interface, as it was recently done in various other South
226 America subduction zones (*Ruegg et al.*, 2009; *Bejar-Pizarro et al.*, 2010; *Moreno et al.*,
227 2010; *Chlieh et al.*, 2011; *Métois et al.*, 2012). The back-slip approach has been shown to be a
228 good approximation, even in the case of non-planar geometry (*Kanda and Simmons*, 2010).
229 The modeled megathrust surface follows the curved slab geometry proposed by *Font et al.*
230 (2013) based on the background microseismicity and results from marine surveys in the area
231 of La Plata Island (*Graindorge et al.*, 2004). The use of a curved geometry rather than a
232 simple single plane fault model is justified by the fact that very shallow dipping subduction
233 interface ($\sim 5^\circ$) is observed close to the trench (*Graindorge et al.*, 2004), with increasing dip
234 further inland, that changes the distance of the GPS sites relative to the subduction interface.
235 It also enables to account for the 25° strike change of the trench axis in the investigated
236 domain. Our fault surface is discretized into 467 elementary subfaults of 11.1 x 11.2km,
237 covering about 250km along strike and extending from the trench to 60km depth. Our model
238 uses a rake fixed to the Nazca/North Andean Block relative motion (Figure 3) and a
239 homogeneous semi-infinite elastic half-space.

240

241 Our inversion scheme follows the approach recently described in *Radiguet et al.*
242 (2011), following *Tarantola* (2005), where we minimize the cost function $S(m)$ defined as :

$$243 \quad S(m) = \frac{1}{2} \left[(Gm - d)^t C_d^{-1} (Gm - d) + (m - m_0)^t C_m^{-1} (m - m_0) \right], \quad (1)$$

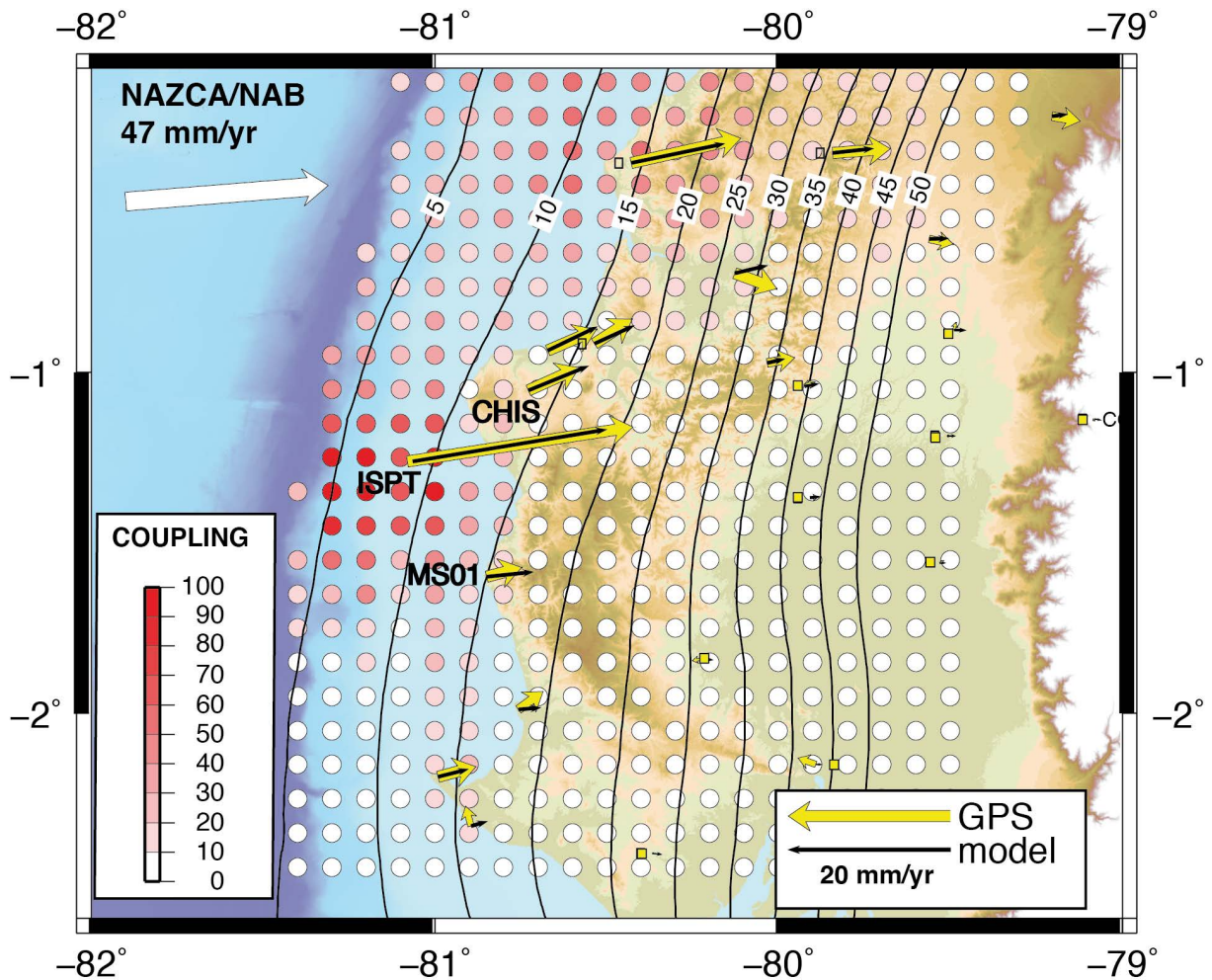
244 where m is the unknown parameter model including the amount of back-slip for each subfault,
245 m_0 is an a priori model for back-slip distribution taken here as 0, d is the vector of observation

246 including the GPS velocity components. G is the transfer matrix including the contribution of
247 each individual subfault back-slip contribution to d . C_d and C_m are the variance-covariance
248 matrices associated with the data and the model respectively. C_d is taken as a diagonal
249 matrix including the standard deviation derived from the geodetic analysis. C_m is taken in the
250 form of :

$$251 \quad C_m(i, j) = \left(\sigma_m \frac{L}{L_0} \right)^2 \exp\left(-\frac{d(i, j)}{L} \right) \quad (2)$$

252 where $d(i, j)$ is the distance between two subfaults i and j , L is the critical distance for
253 correlation for slip, and L_0 is a scaling factor fixed at 10km. σ_m is taken as the maximum
254 possible velocity (48mm/yr). We show the results obtained for $L=50$ km, which is found to be
255 a good value between the roughness of the model and the misfit to the observed GPS
256 velocities.

257



258

259

260 *Figure 3: Map of spatial distribution of coupling along the Central Ecuador subduction zone.*

261 *Yellow arrows show observed GPS velocities derived from both continuous and campaign*

262 *measurements. Velocities are expressed with respect to the North Andean Block (NAB).*

263 *Locations of GPS sites with small velocities are shown by the yellow squares. The three*

264 *stations discussed in the text (ISPT, CHIS, MS01) and the iso-depth of the subduction*

265 *interface are indicated on the map (from Graindorge et al. (2004) and Font et al. (2013)). The*

266 *modeled velocities (black arrows) correspond to the optimal spatial distribution of coupling*

267 *along the subduction interface shown by the color circles. Circle color indicates the level of*

268 *coupling (see color scale).*

269

270 The inversion reveals the existence of a local (50 x 50km) highly coupled area below
271 La Plata Island and extending up to the trench (Figure 3). The high level of coupling is
272 required to explain the velocity of 28.5 ± 0.5 mm/yr at Isla La Plata station ISPT. The downdip
273 extension (~15km) of the locked fault zone is well constrained by the sharply decreasing
274 velocities from ISPT to CHIS (8.8 ± 0.5 mm/yr) and MS01 (5.4 ± 1.5 mm/yr), both located at
275 about 70km from the trench. Along strike extension of the high coupling area is constrained
276 by the increasing northwards component of velocity at station CHIS and its surrounding.
277 Station MS01 rules out any significant coupling at depth ~15km at latitude 1.5°S, but cannot
278 exclude any significant coupling close to the trench (See *Chlieh et al.*, in preparation, for
279 more details regarding the interseismic coupling models and spatial resolution tests).

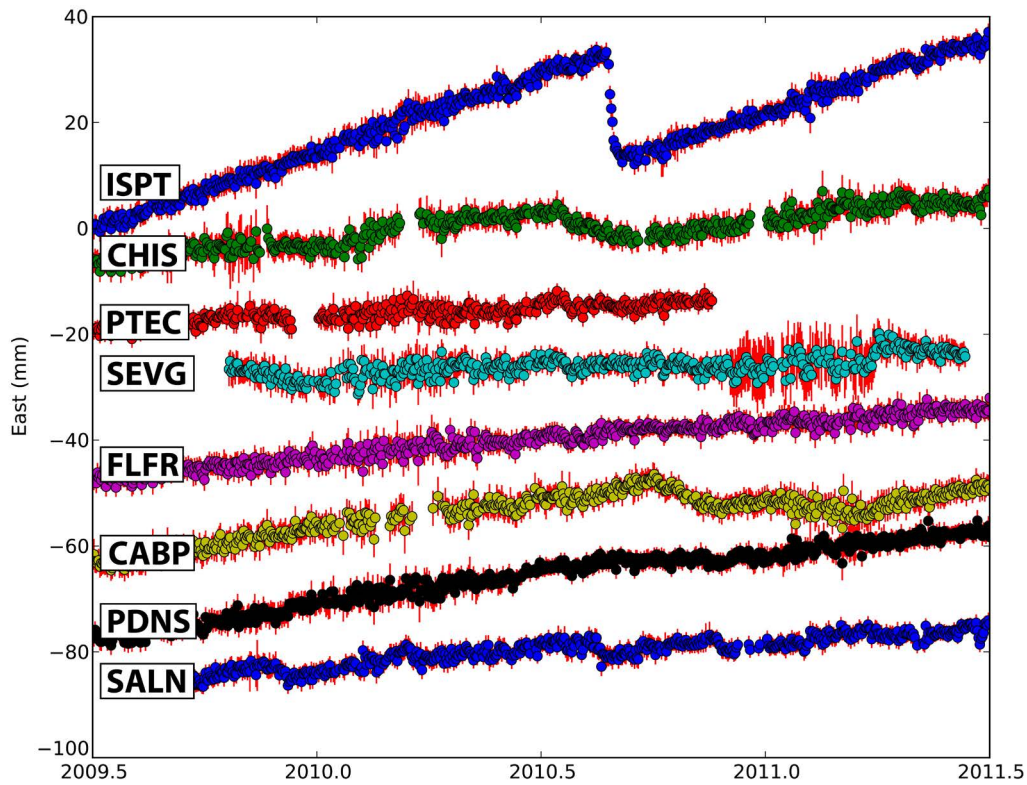
280

281 **3) Slow slip observation and modeling**

282

283 Figure 4 shows the East component time evolution of the continuous GPS sites
284 expressed in the NAB reference frame. In this framework, the trends of increasing East
285 displacement through time directly witness the elastic effect of interplate coupling along the
286 subduction interface. Time series have been corrected for the common mode network motion
287 (*Wdowinsky et al.*, 1997). They typically have weekly repeatability of the order of 1-2mm
288 enabling to have a precise monitoring of short-term transient.

289



290

291 *Figure 4: Continuous GPS Time series (East component) for the 2009.5-2011.5 period.*

292 *Formal errors are shown by red lines (1-sigma confidence level). Daily positions (circles)*

293 *are with respect to the North Andean Block. Clear reversal of the interseismic deformation is*

294 *observed during 6 days at ISPT, during the summer 2010.*

295

296 At station ISPT, the time series clearly show a $\sim 2\text{cm}$ rapid progressive westwards

297 displacement detected from the 26th of August 2010, decelerating from the 30th of August

298 2010 for a few days, before recovering a constant rate interseismic displacement. Mainly

299 because of the lower precision of the GPS on the vertical component, no clear progressive

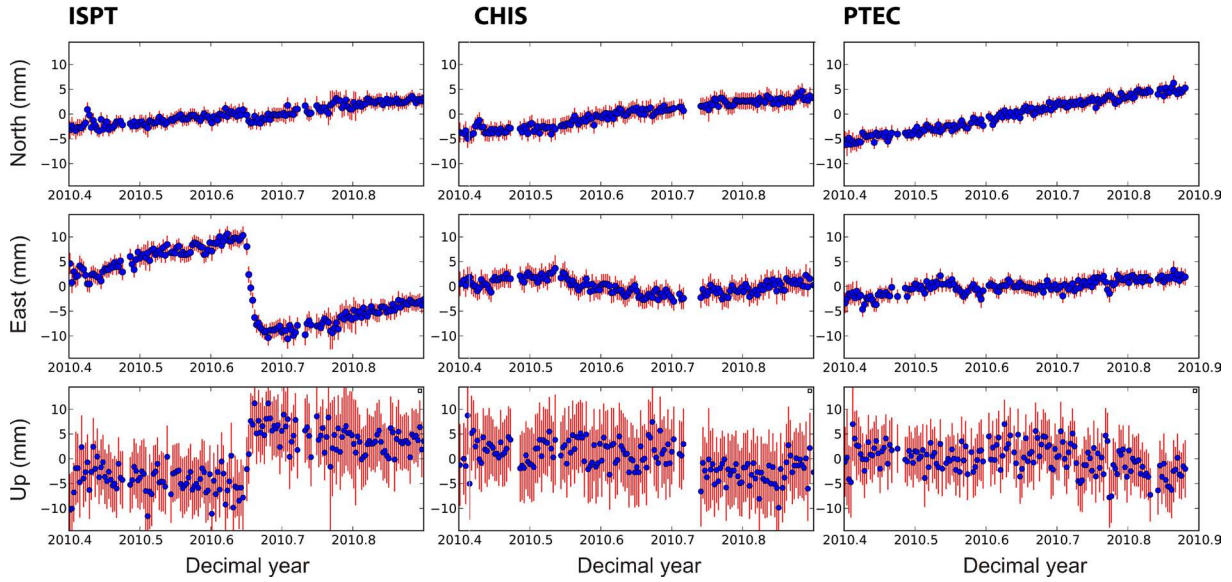
300 motion is seen on the vertical component (Figure 5). Nonetheless, we average the position 5

301 days before and after the SSE and find a total displacement of -19.6 ± 1.1 , -2.0 ± 1.0 ,

302 $11.25 \pm 3.3\text{mm}$ on the East, North and Up component respectively (uncertainties are $1-\sigma$

303 confidence interval). During the same period of time, no significant displacement is found
 304 neither at the closest station to ISPT, CHIS, nor at PTEC (see location of the stations in Figure
 305 1 and their three-component displacements in Figure 5).

306



307

308 *Figure 5: Time series for the 3 continuous GPS sites used in the search of the SSE*
 309 *parameters. Positions are shown by circles and associated formal errors by red lines (1-*
 310 *sigma confidence level). The SSE is clear on the East and vertical components of ISPT, but*
 311 *its signal is very small on the North component of ISPT, as well as on all the components of*
 312 *CHIS and PTEC.*

313

314 With only one site having significant displacement during the SSE, any proper
 315 inversion of the slip distribution is excluded. Nonetheless, we can examine the constraints
 316 provided by the data at stations ISPT, CHIS, and PTEC in order to evaluate the range of
 317 models able to explain them. In order to reduce the number of parameters to be searched, we
 318 use an a priori model of the slip distribution in the bi-dimensional Gaussian form:

319

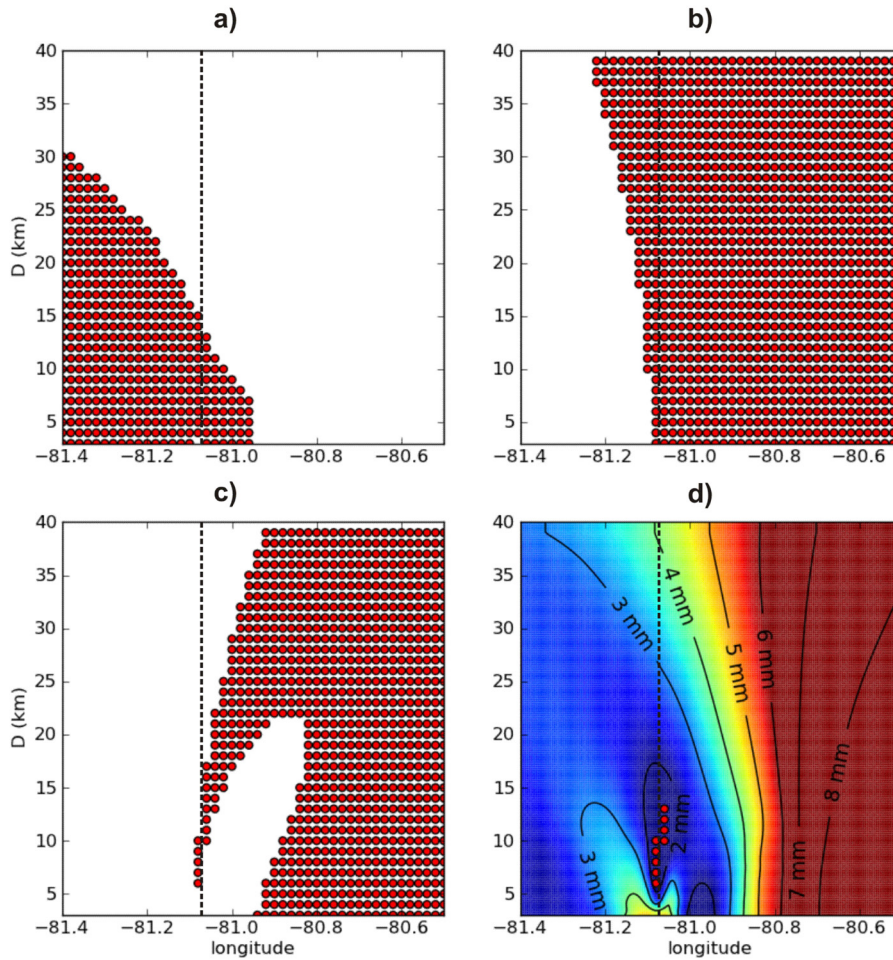
$$320 \quad s(\lambda, \phi) = s_{\max} \exp\left[-R_t^2 (\cos^2 \phi_0 (\lambda - \lambda_0)^2 + (\phi - \phi_0)^2) / D^2\right], \quad (3)$$

321 where s is the slip along the subduction interface at longitude λ and latitude φ (expressed in
322 radians). (λ_0, φ_0) is the location of maximum slip, R_t is the radius of the Earth, and D is the
323 characteristic radius of significant slip. The rake is fixed at 90° . We then examine the
324 constraints provided by the total displacement observed at ISPT and the null displacements at
325 the nearby sites CHIS and PTEC (taken at the precision of the GPS, here found to be 1.1mm
326 on the horizontal components at CHIS and PTEC and 3.9mm on the vertical component, at
327 the 1- σ confidence level).

328

329 The first constraint is that very small North component of displacement is found at
330 ISPT. That means that, either the motion was homogeneous over a large area surrounding the
331 site ISPT or that the slip was at the first order symmetrical either side of the ISPT site. The
332 lack of displacement noticed at CHIS favors the latter hypothesis. φ_0 was therefore kept fixed
333 to the latitude of ISPT, that is, we search for possible slip distribution models whose center
334 lies along a line going through the location of ISPT in an east-west direction. We sample the
335 model space, by varying λ_0 from the trench (81.4°W) to 80.5°W and varying D from 3 to
336 40km. For each (λ_0, D) , s_{max} is a simple scaling factor that can be directly estimated using a
337 least-squares inversion. Using this formulation, we investigate how the observations constrain
338 the range of possible models (Figure 6).

339



340

341 *Figure 6: Exploration of the possible spatial parameters of the SSE. All subfigures show the*
 342 *acceptable models by red dots, in the bi-dimensional parameter space (λ_0 :longitude; D:*
 343 *radius of the slip). The longitude of station ISPT is shown by the vertical dashed line. a), b),*
 344 *and c) show how some specific features of the observed displacements forbids some parts of*
 345 *the parameter space (see main text). d) shows the location and size of the slow slip patch*
 346 *verifying the 3 constraints a-c. Weighted root mean square values (in mm) of misfit are shown*
 347 *by the contours and the color scale with increasing values from blue to red.*

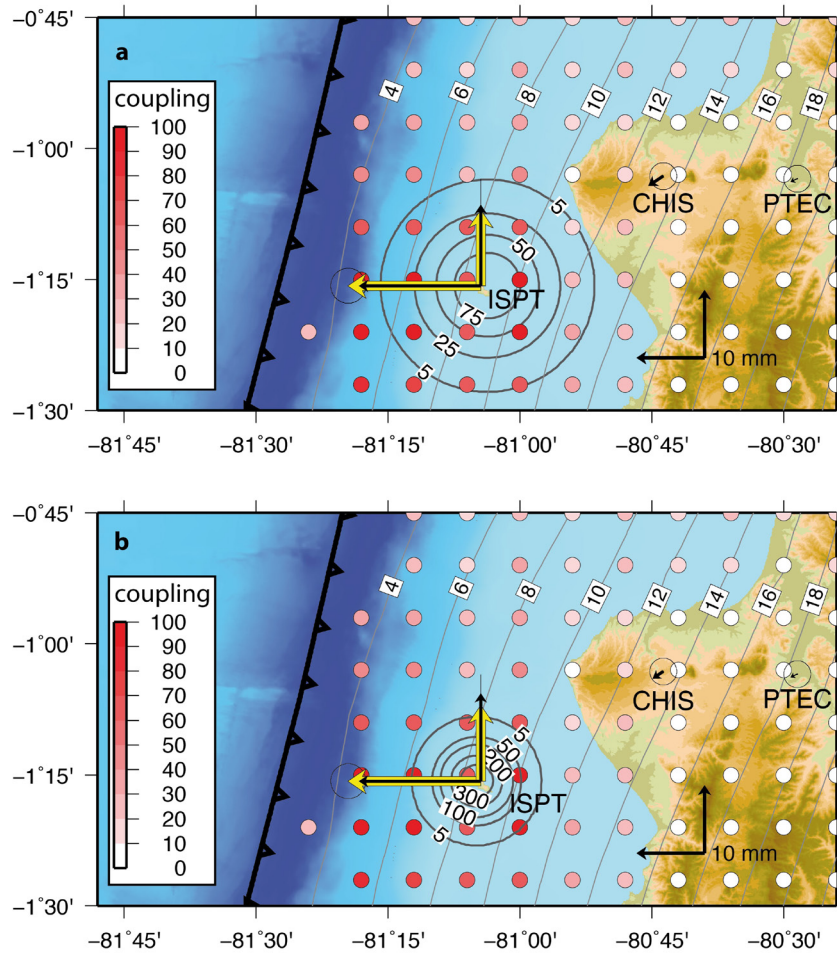
348

349 The absence of any significant displacement detected at CHIS and PTEC excludes any
 350 significant amount of slip below the coastline or inland. Figure 6a shows the acceptable
 351 region of the parameters space, which meets the criterion of 2cm eastwards displacement at
 352 ISPT and a null displacement at CHIS and PTEC (at the 3- σ confidence level). The second

353 constraint is the upwards displacement observed at ISPT. Analytic solutions for a 2-D thrust
354 buried dislocation (e.g. *Freund and Barnett (1976)*, *Rani and Singh (1992)*, *Tomar and*
355 *Dhiman (2003)*, *Cohen (1999)*, *Chlieh et al. (2008)*) indicate that, for a buried thrust fault,
356 vertical surface displacements are predicted to be upwards on the updip side of the dislocation
357 and downwards on the downdip side, the transition between the two regimes occurring above
358 the dislocation. Figure 6b shows the region filling the criterion of upwards displacement at
359 ISPT. Taken together, these two constraints limit the range of possible slip area from about
360 81.12°W to 80.96°W and a characteristic radius below 18km. A final constraint is provided
361 by the ratio between the Up and East displacements which is of the order of -0.5. Taking the
362 uncertainties into account, this ratio is considered acceptable in the range [-0.77 -0.38].
363 Respecting such a ratio range indicates two possible ranges of slip location with respect to
364 ISPT (Figure 6c). One class of models corresponds to slip located in the very near vicinity of
365 ISPT, in agreement with the previous constraints. The second class is obtained for slip located
366 further east of ISPT, that can be discarded due to the absence of slip observed at station CHIS.
367

368 Taking all these constraints into account, we find that the range of possible values is
369 rather narrow: the longitude λ_0 of maximum slip is located between 81.08°W and 81.06°W
370 and the characteristic slip radius D is in the range [6km 13km] (see Figure 6d). For any
371 solution belonging to these intervals, the weighted root mean square is below 2mm, therefore
372 in agreement with the GPS displacements uncertainties. The amount of maximum slip s_{max} is
373 not well resolved, ranging between 97mm and 407mm. Moreover, this is a local value that
374 may not be very representative of the global process. Averaged over the area where it is larger
375 than 5% of its maximum, slip is found in the range 50mm-200mm. The moment is better
376 resolved and always remains in the range of $M_w = 6.0-6.1$ (using a classical rigidity of

377 30Gpa). Figure 7 shows the slip distribution for the two extreme models. ($\lambda_0 = 81.06^\circ\text{W}$, $D =$
 378 13km and $\lambda_0 = 81.08^\circ\text{W}$, $D = 6\text{km}$).
 379



380
 381 *Figure 7: Map view of the two extreme possible slip models. (a) Model corresponding to a*
 382 *characteristic slip radius of 13km and a maximum slip of ~10cm. (b) Model corresponding to*
 383 *a characteristic slip radius of 6km and maximum slip of ~40cm. Thick yellow and thin black*
 384 *arrows are observed and modeled displacements respectively (horizontal and vertical*
 385 *components). Numbers along the concentric circles indicate isovalues of slip (in mm). Depth*
 386 *contours of the subduction interface and coupling spatial distribution are indicated as in*
 387 *Figure 3. Both models indicate that the area of major slip occurred within the deeper part of*
 388 *the area coupled during the interseismic phase, with possible slip extending in the partially*
 389 *coupled area for extreme model b).*

390 Our parameter search shows that the main area of slip is located close to the downdip
391 limit of the interseismically highly coupled area (Figure 3). Slip extending at greater depth in
392 the partially coupled area is possible for some extreme models, but the range of acceptable
393 radius found in the grid search prevents any further quantification. However, our parameter
394 grid search rules out any slip distribution occurring from the trench to the downdip limit of
395 the locked zone, or even any slip distribution centered west of ISPT. In terms of moment
396 release, our search does not account for along strike extension of the slip. We might therefore
397 underestimate the moment release, as an aspect ratio of 3 would increase the moment
398 magnitude by 0.2-0.3. Taking this into account, the equivalent moment magnitude (M_w)
399 released during the 2010 SSE is found to be in the range of 6.0 to 6.3.

400

401 **4) Properties of the associated seismicity**

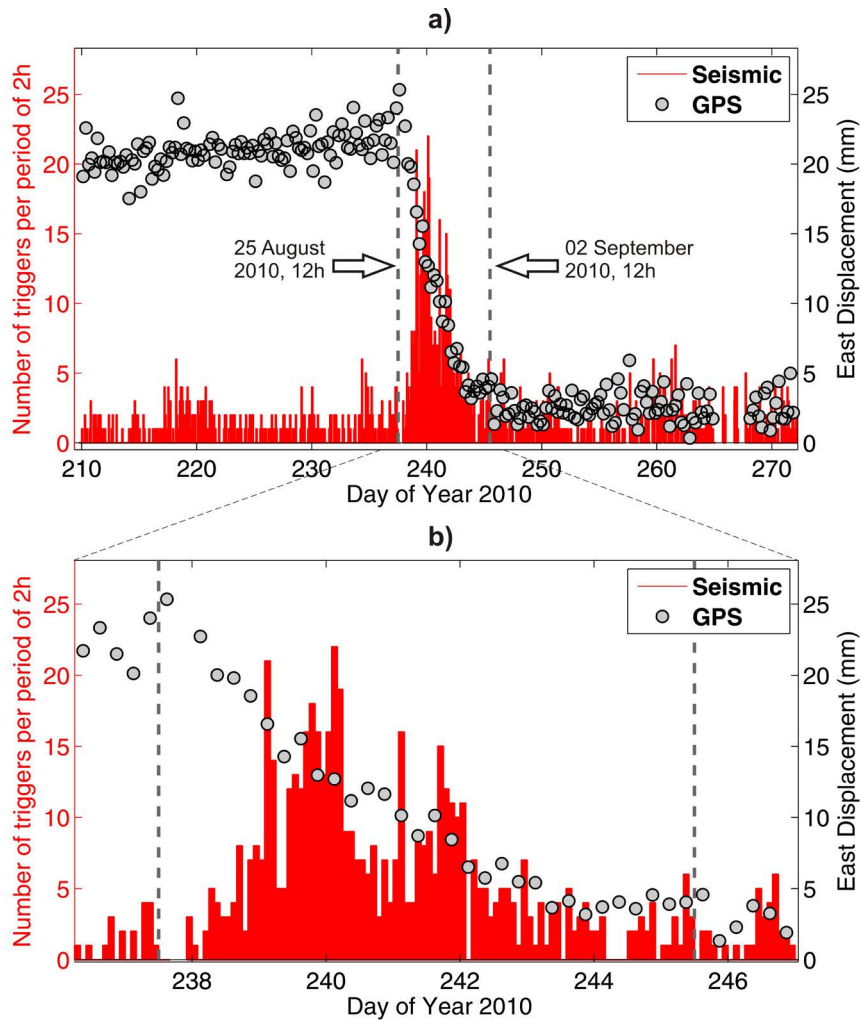
402

403 **4.1) Evidence of intense seismic activity**

404

405 Visual screening of data recorded at station ISPT shows a rate of seismic events higher
406 than usual during the period of occurrence of the SSE. To quantify this increase of activity,
407 we applied to the continuous data a LTA/STA detection algorithm using a LTA of 60s and a
408 STA of 1s. The counting of events detected using this technique is presented in Figure 8,
409 conjointly with the GPS displacements calculated every 6 hours. Despite a relatively high
410 background number of detections mainly related to oceanic noise, the curve clearly points out
411 an increase of seismic activity during the SSE. The seismic activity does not start before the
412 beginning of the SSE, and thus does not appear to have a role in the SSE initiation. The period
413 of strongest seismic activity (26/08-29/08) correlates very well with the period of fastest
414 displacement observed at the GPS station. During these four days, several distinct peaks in the

415 number of events are visible, showing variations of seismic activity during the SSE itself.
 416 Most of the events are not detected at other stations of the ADN array, located about 120km
 417 away for the closest ones (CABP and SEVS, see Figure 1), which indicates that the seismicity
 418 is dominated by local and low-magnitude earthquakes.



419
 420 *Figure 8: Joint observations of the geodetic displacement and of the seismicity rate at La*
 421 *Plata Island (ISPT station) during the 2010 SSE. (Red) Number of seismic events detected*
 422 *over 2 hours sessions for an LTA/STA ratio higher than 6.0. (Grey dots) East displacement*
 423 *recorded by the GPS station, calculated every 6 hours. a) shows the time window starting 4*
 424 *weeks before the SSE and ending 4 weeks after the SSE. b) is a zoom detailing seismic activity*
 425 *and geodetic displacement during the SSE. In both subfigures the left and right dashed lines*
 426 *indicate the dates of 25 August 2010 (12h) and 2 September 2010 (12h), respectively.*

427 The visual shape of the waveforms confirms the local character of the seismicity. Most
428 events show clear P and S arrivals, with a time difference of the order of 1.5-3s. The
429 impulsive arrivals of the waves do not differ from those of local earthquakes regularly
430 recorded along the Ecuadorian coast. While this “classical” seismicity increase is very clear
431 during the SSE, it also seems that no tremor-like activity has been triggered. Both visual
432 screening of the seven-day long sequence and analysis of the energy variations in successive
433 time windows (*Payero et al.*, 2008) do not indicate peculiar features. Even if some minor
434 tremor activity might be discovered by refined analyses (*Kim et al.*, 2011), it clearly appears
435 that the regular earthquakes with impulsive waves arrival define the main seismic process
436 associated with this SSE.

437

438 In the following paragraphs, we therefore concentrate on the properties of this
439 associated seismicity. Two approaches are considered. We first use the three components of
440 the broad-band station ISPT to locate and characterize the largest events of the seismic
441 sequence. This reduces the analyzed activity to a total of about 50 events. In a second time,
442 we perform waveform classification based on cross-correlation techniques. Such an approach
443 does not provide the absolute source parameters, but has the double advantage of (1) giving a
444 robust estimate of the number of tectonic events (while LTA/STA detection procedure may
445 also identify various technical artifacts) and more importantly (2) enlightening how part of the
446 seismicity is organized in terms of repeating events.

447

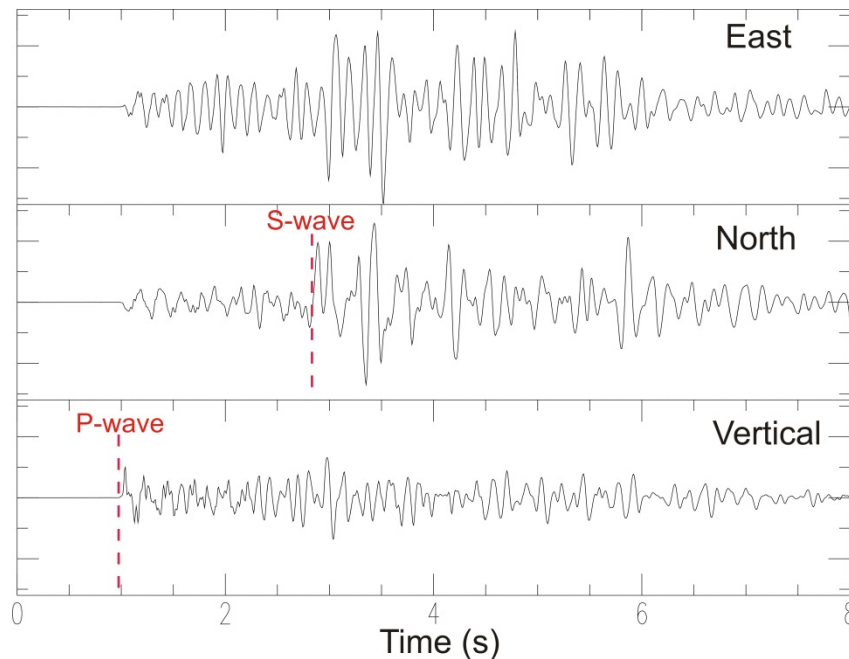
448 **4.2) Location and source properties of the largest events**

449

450 Because most events are only recorded by station ISPT, we cannot use standard phase
451 picking techniques to locate them. However, the events exhibit clear P and S wave arrivals,

452 with a small time difference between P and S waves and a large P wave amplitude on the
453 vertical component (Figure 9). This indicates that a large number of earthquakes has an
454 epicenter close to the La Plata Island. We can therefore estimate the earthquakes location by
455 studying the particle motions at ISPT station (see e.g. *Alessandrini et al.*, 1994, and references
456 therein). We first determine the back-azimuth of the earthquake by rotating the horizontal
457 components and finding the orientation that minimizes the waveform energy along one of the
458 rotated components. Using this information, we repeat the previous operation with the radial
459 and vertical components to retrieve the incidence angle of the P wave (see illustration and
460 more information about this procedure in Supplementary Figure A.1). Finally, the differential
461 time between P and S waves allows us to estimate the location of the earthquake along the P-
462 ray.

463



464

465 *Figure 9: Typical local earthquake waveforms (in velocity) recorded at ISPT station (origin*
466 *time of the event : 2010/08/27, 08h57m15s). The three components are shown at the same*
467 *scale.*

468

469 The variations of the crustal wave velocities add some complexity to this simple
470 approach. In this study, we neglect the effects of the lateral variations and only consider the
471 dominant effects of wave velocities increasing with depth. In this one-dimensional model, the
472 back-azimuth determination is not affected. The incidence angle determination is made more
473 difficult, because the radial component includes both the direct P wave and P-S waves
474 refracted below the station. If using unfiltered signals over a duration including some P-S
475 waves, the determination of the incidence angle is biased by these different wave types
476 arriving on the vertical and radial components. If using very short time windows close the
477 first P wave arrival, the determination is less stable and only reflects the incidence angle in the
478 very shallow part of the crust. To obtain a more robust value, we band-pass the signal
479 between 1Hz and 4Hz, and use the first 0.4s following the P wave arrival. Such a filtering
480 reduces the potential number of analyzable earthquakes, because of the low signal-to-noise
481 ratio for small events waveforms low-passed at 4Hz. Based on amplitude criteria, we finally
482 select 49 earthquakes for which the determination of back-azimuth and incidence angles is
483 reliable.

484

East of ISPT			West of ISPT		
Depth (km)	P velocity (km/s)	S velocity (km/s)	Depth (km)	P velocity (km/s)	S velocity (km/s)
0-2	4.3	2.48	0-5	4.3	2.48
2-	6	3.46	5-	6	3.46

485

486 *Table 1 : One-dimensional models used to locate the associated seismicity.*

487

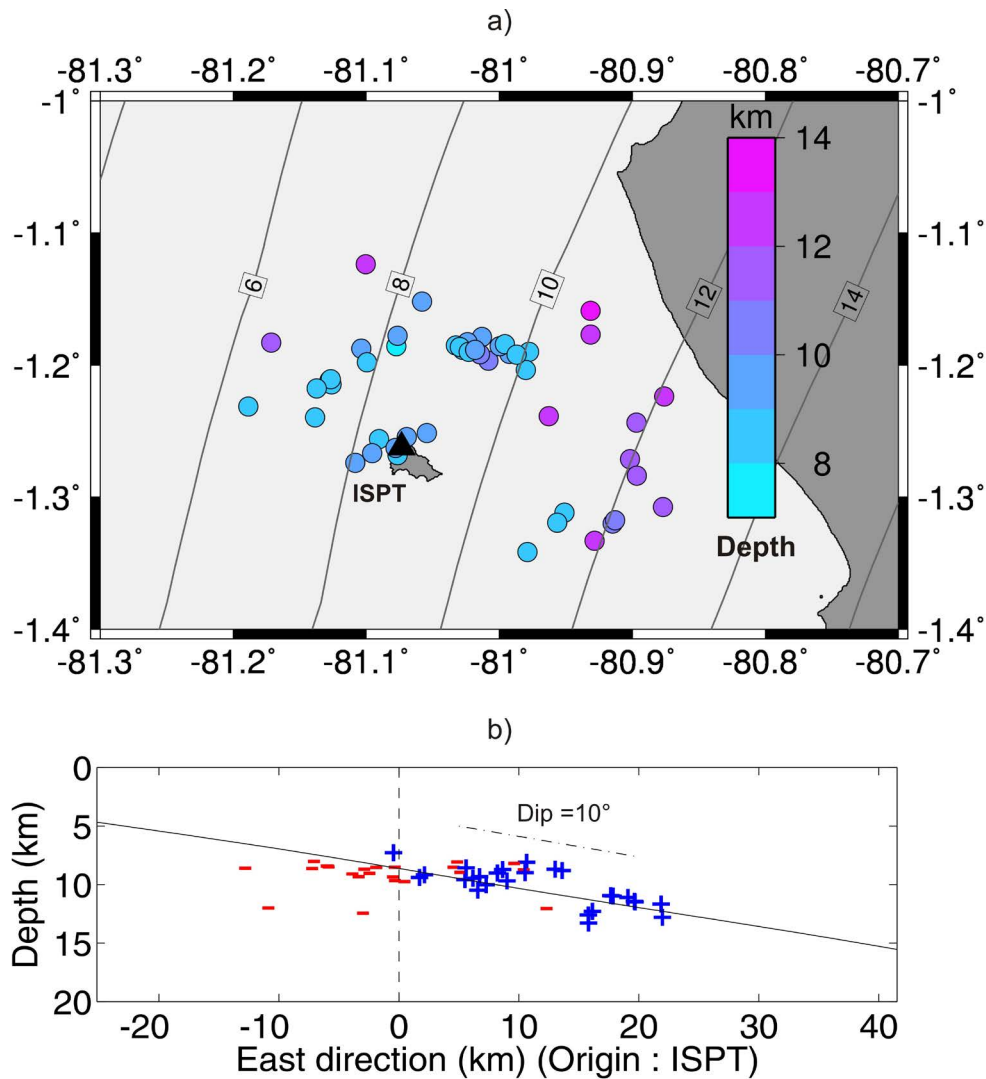
488 The location of the hypocenter along the P-ray is more directly dependent on the wave
489 velocity structure. To estimate its realistic variation close the La Plata Island, we use the study
490 of *Graindorge et al.* (2004), who have derived an East-West crustal model by inversion of

491 wide-angle seismic data. This profile is located only 15km South of La Plata Island, and is
492 therefore well adapted to the present study. The depth of interplate seismicity, observed
493 during a seismic experiment (SISTEUR, *Béthoux et al.*, 2011), was shown to be consistent
494 with the *Graindorge et al.* (2004) model. It reveals that, below the La Plata Island, solid
495 crustal rocks (“Piñon” formation, with P wave velocities of the order of 6-6.5km/s) are
496 already present at 2-5km depth. This is a favorable configuration for the location technique, as
497 the ray geometry of the P wave should remain simple between the subduction interface and
498 superficial depths. Based on the *Graindorge et al.* (2004) model, we derive two average
499 layered models (presented in Table 1) to take into account that the top of the Piñon formation
500 is deeper West of ISPT. Depending on the back-azimuth, we select the corresponding model
501 to locate the hypocenter along the P-ray using the differential S-P time.

502

503 In Figure 10, we present the obtained hypocentral locations, both in map and projected
504 along a West-East vertical plane. The depth locations for earthquakes located below ISPT (8-
505 10km) are in good agreement with the depth of the subduction interface determined by
506 *Graindorge et al.* (2004). These depths are little affected if using different realistic velocity
507 values for the first layer, because the ray is almost vertical. Depths for earthquakes East of
508 ISPT are more sensitive to the first layer parameters, as faster velocities inside this first layer
509 lead to steeper rays, then resulting in deeper hypocenters. However, all models result in an
510 increasing depth for earthquakes located more inland, in agreement with events occurring on
511 or close to the subduction interface. Using the model presented in Table 1, the best average
512 dip East of ISPT is found to be equal to 10° , the same value as in the *Graindorge et al.* (2004)
513 model. In Figure 10b, we add to the depth location the polarities read on the vertical
514 component of the ISPT station. As expected for thrust earthquakes occurring on an almost flat
515 interface, most polarities are positive East of ISPT and negative West of ISPT. These

516 elements are consistent with a typical release of the stress accumulated during the interseismic
517 period.



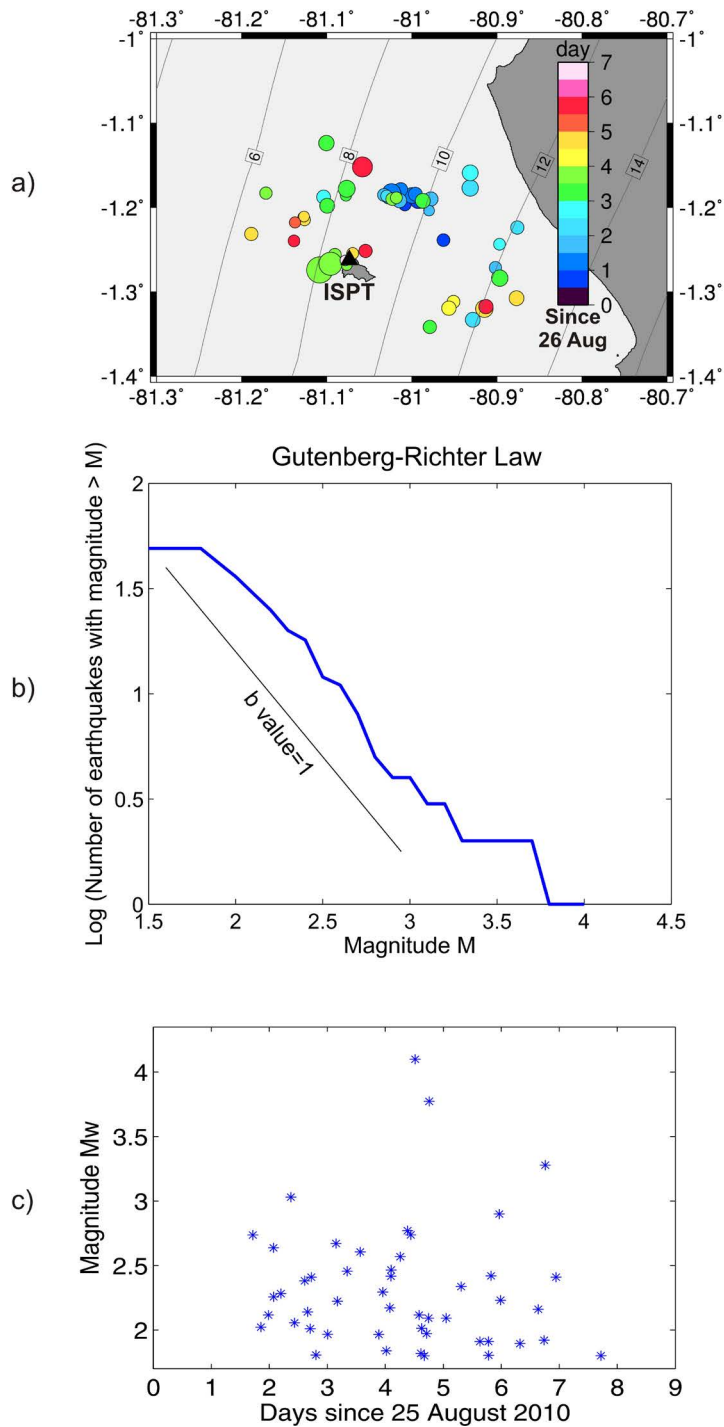
518

519

520 *Figure 10 : Hypocentral location of the largest events : a) Map location with color scaled to*
521 *depth. The annotated contours indicate the depth of the subduction interface as in Figure 3. b)*
522 *Projection on the West-East vertical plane. The black line represents the subduction interface.*
523 *The optimal linear fit of the events East of ISPT defines a 10° dip (dash-dotted line).*
524 *Polarities on the vertical component of the ISPT broadband station are shown in the cross-*
525 *section.*

526

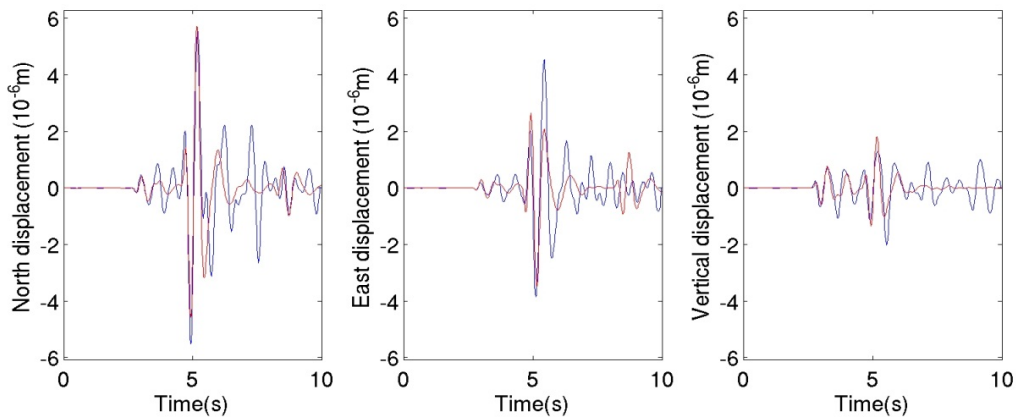
527 The magnitude distribution can be estimated by modeling the waveforms of the
528 earthquakes. We invert the waveforms - filtered in the [1Hz 2.5Hz] range – to retrieve the
529 mechanism and moment magnitude, using a window starting at the P wave arrival and ending
530 1s after the S wave. To do so, we have developed an inversion scheme based on the wavefield
531 modeling by the discrete wavenumber method (*Bouchon*, 1981). The mechanism
532 determination may be ambiguous, but the magnitude is expected to remain meaningful. Figure
533 11a shows the location map of the associated seismicity, with circle sizes scaled to the
534 moment magnitude and colors depending on the occurrence date. We observe that the
535 seismicity started on 26 August close the location (81°W , 1.2°S), before migrating, mostly
536 West and South, in the following days. When analyzing the classical magnitude scaling laws
537 (Figure 11b and 11c), we note that the Gutenberg-Richter law is well respected with a
538 classical b-value close to 1. On the other hand, Figure 11c shows that the seismicity does not
539 follow a mainshock-aftershock behavior (Omori's law): large and small magnitude events
540 appear to occur randomly, with the largest shocks ($M_w=3.8$ and 4.1) occurring on August
541 29th, several days after the beginning of the sequence. This observation is a further evidence
542 that the seismicity is driven by an external cause – here the SSE -, and not by internal stress
543 interaction.



544

545 *Figure 11 : Magnitude and time distribution of the associated seismicity. a) Map location,*
 546 *with color scaled to occurrence date and size to moment magnitude (M_w). The smallest*
 547 *circles are events of $M_w=1.8$ and the largest one is a $M_w=4.1$ earthquake. The depth of the*
 548 *subduction interface is contoured and labeled (in km) as in Figure 3. b) Gutenberg-Richter*
 549 *law with the classical b-value slope (equal to 1) presented on the left part of the figure. c)*
 550 *Distribution of magnitude as a function of occurrence time.*

551 As the focal mechanism may be unreliably retrieved by the analysis of only one
 552 seismic station, we adopt a different strategy to further check that the seismicity is consistent
 553 with a thrusting mechanism along the interface: in the inversion process, we restrain the
 554 possible range of focal mechanism angles (in such a way that only realistic interface thrust
 555 earthquakes can be modeled), and evaluate if the real waveforms can be adequately matched.
 556 We present in Figure 12 an example of waveforms modeling (same earthquake as in Figure
 557 9), illustrating that P and S waves are satisfactorily modeled, on the three components, by a
 558 typical subduction mechanism. For the earthquakes with $M_w > 2.5$, we found that 9
 559 earthquakes over 12 have both their polarities and waveforms in agreement with inverse slip
 560 on the subduction interface.
 561



562
 563
 564 *Figure 12 : Comparison between displacements recorded at ISPT station (blue) and*
 565 *synthetics (red), for the 2010/08/27, 08h57m15s, event (see raw data in Figure 9). Both data*
 566 *and synthetics are band-pass filtered between 1Hz and 2.5 Hz. This earthquake has been*
 567 *located at (Latitude, longitude, depth) = (1.19°S, 81.02°W, 9.5km) by the location procedure.*
 568 *The source parameters corresponding to synthetics are (strike,dip,rake)= (13°,9°,80°) and*
 569 *$M_w=3$. The good agreement between data and synthetics shows that this earthquake is*
 570 *consistent with a thrust mechanism along the subduction interface.*

571 As shown in Figure 11, the largest events of the sequence are two earthquakes of
572 moment magnitude equal to 3.8 and 4.1. We estimate the cumulated moment released by the
573 smaller earthquakes by integrating the Gutenberg Richter law (see *Andrews and Schwerer,*
574 2000), and obtain an equivalent moment magnitude of 3.7. As a whole, the seismicity released
575 a seismic moment equivalent to a $M_w=4.2$ earthquake, much smaller than the moment
576 magnitude of the SSE (M_w larger than 6.0). In terms of moment ratio, the cumulative moment
577 released through earthquakes accounts for 0.1-0.2% of the total moment release. Together
578 with the location, timing and mechanism analysis, this observation is fully consistent with a
579 slip on the subduction interface mostly accommodated by the SSE, which has itself
580 seismically triggered small locked patches, located on or very close to the interface. To better
581 characterize the behavior of these locked patches, we now specifically analyze how the whole
582 triggered seismicity (and not only the largest earthquakes) is organized in terms of repeating
583 events.

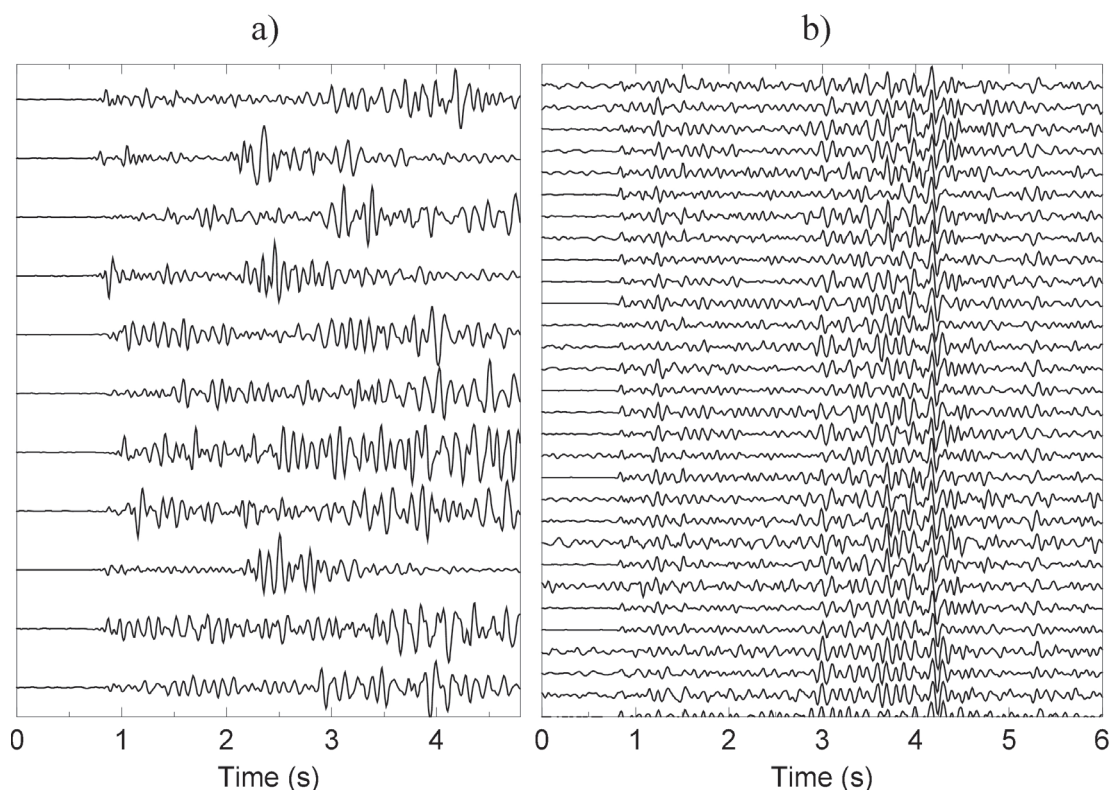
584

585 **4.3) Organization of the seismicity**

586

587 We now select all triggers with a LTA/STA higher than 4.0 between 2010/07/28 and
588 2010/10/06 and in addition those with a LTA/STA between 3.0 and 4.0 between 2010/08/25
589 and 2010/09/02. The choice of such low detection thresholds enables the detection of small
590 amplitude events, but has the drawback of also selecting numerous noisy traces that will be
591 disregarded later in the processing. For the 8971 triggers, we extracted for the vertical
592 component of ISPT windows with a 2048-sample (16.4 s) length starting 500 samples (4 s)
593 before the triggering times. All waveforms have been compared one to each other using
594 cross-correlation after filtering between 3 and 17 Hz. We consider that an event belongs to a
595 family if it has a correlation higher than 0.80 with at least one of the other events. The

596 classification indicates the presence of 34 families of similar tectonic earthquakes (Figure 13)
597 including more than 5 events and grouping a total of 270 earthquakes. 30 of these families
598 only include events which occurred during the SSE. Additionally, 406 earthquakes are
599 grouped in smaller families of less than 5 events. This procedure allows the determination of
600 the main active clusters during the SSE and during the few months around. The similarity of
601 waveforms guaranties that events belonging to a same family have both similar hypocentral
602 locations and source characteristics.



603

604

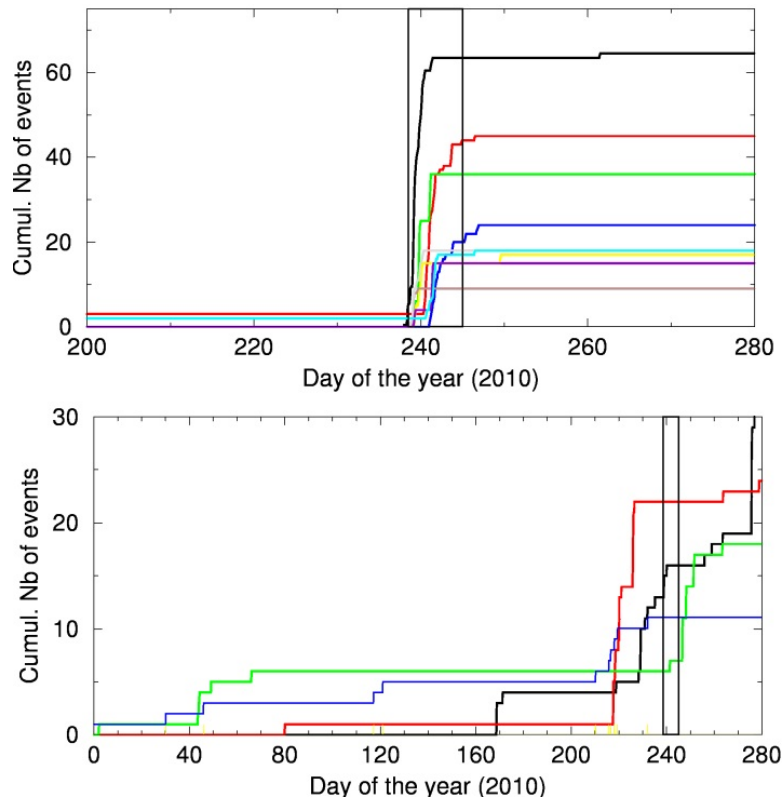
605 *Figure 13: a) Examples of reference stacks used to scan the data. b) Examples of similar*
606 *waveforms detected for the largest family active during the SSE.*

607

608 To recover precisely the time history of the 34 largest families over a duration longer
609 than that of the SSE, as well as to identify events possibly missed in the detection or in the
610 classification, we scan the data using a matched-filter technique. We generate for each family

611 a synthetic waveform of 600 samples (4.8 s) obtained by stacking all similar events (Figure
612 13). These waveforms, calculated for the vertical component of ISPT, include for most of
613 them both P and S phases indicating hypocentral distances between 10 and 20km. The stacks
614 are used to scan the data by sliding the reference waveforms along the continuous data in
615 search of similar signal windows. The scanning is performed after band-pass filtering both the
616 reference traces and the continuous data between 3 and 17 Hz. We analyze the entire period
617 from 2009/07/08 to 2010/10/06. To detect a maximum number of events similar to the
618 reference stacks, we consider as similar each time window with a cross-correlation higher
619 than 0.7. The procedure now allows to significantly increase the number of events involved in
620 each family, since, for the chosen correlation threshold, 573 events are now involved in the 34
621 main clusters. For 30 of the families, temporal distributions are similar to those shown in
622 Figure 14 (top), with most of the events occurring only during the SSE. On the contrary, the 4
623 remaining clusters are active indifferently of the occurrence of the SSE. This result shows that
624 specific seismogenic structures are activated only during the SSE.

625



626

627

628 *Figure 14: Upper plot shows, for the 10 largest families active during the SSE, the cumulated*

629 *number of events detected since 2009/07/08. Lower plot shows similar cumulated numbers for*

630 *families active during months around the SSE. In both plots, the period of activity of the SSE*

631 *is between the two vertical black lines.*

632

633 Comparing with the 49 earthquakes located in section 4.2, we directly find that 11 of

634 these larger earthquakes belong to one of the 30 main families. Two pairs of located

635 earthquakes belong to a same family, which informs us on the internal quality of the location

636 procedure: we find that the locations differ by about 1km for earthquakes belonging to the

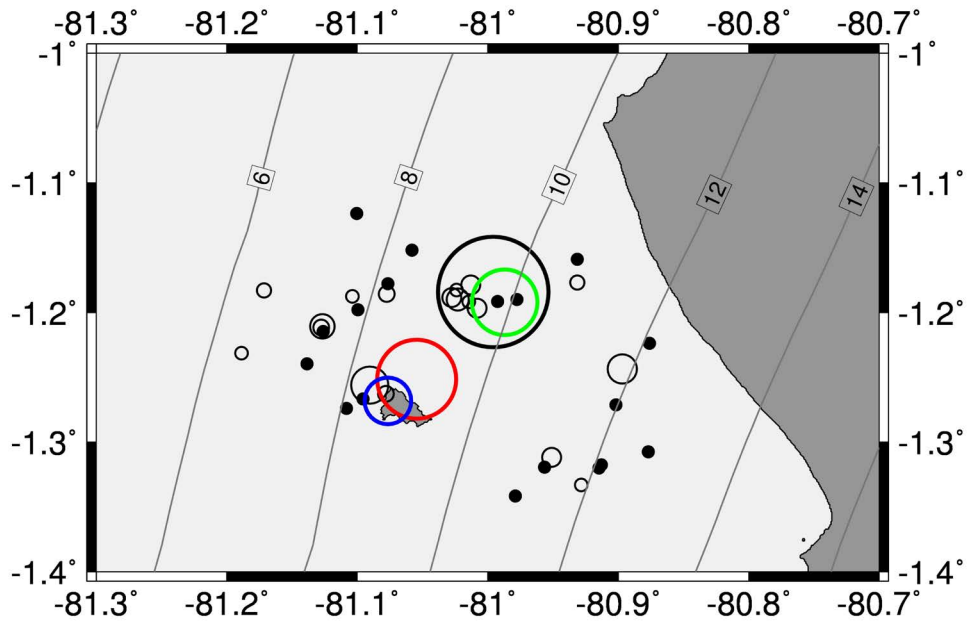
637 same family. Using again the matched-filter technique, we further check if some of these

638 larger earthquakes are really orphans or if the occurrence of repeating similar events is the

639 rule for this triggered seismicity (Figure 15). We find that 23 earthquakes cannot be

640 associated with more than one event. The 6 largest earthquakes (with Mw larger or equal than

641 2.8) belong to this group in which events occur as singlets or doublets. The other earthquakes
642 present a repeating character, which can be moderate (10 earthquakes can be integrated in
643 families of less than 10 events), or very active: 4 earthquakes belong to families of more than
644 20 events (colored circles in Figure 15), the largest one grouping 65 events (see also Figure
645 14). These observations show that the SSE triggers different types of seismicity. Part of it can
646 be understood as immediate stress release on locked patches of the interface, resulting in
647 orphan events. The largest earthquakes belong to this category, and illustrate the triggering
648 potential of SSE for large interplate earthquakes. The events grouped into families indicate
649 that the stress release on some areas of the interface is more complex, with the conjugate
650 effect of SSE stress loading and earthquake interaction. We present in Figure 16 the temporal
651 activation of the 4 main families. As for the whole sequence, the magnitude occurrence inside
652 each family as a function of time does not follow a simple law. This observation suggests that
653 the time-dependent stress induced by the SSE is the dominant triggering factor and that a
654 small seismogenic area progressively ruptures as stress increases with time. However,
655 earthquake interaction also plays a role in the seismicity rate inside a family. This is clear for
656 family 1, where higher seismic activity is present just after the largest earthquake of this
657 family (Figure 16).

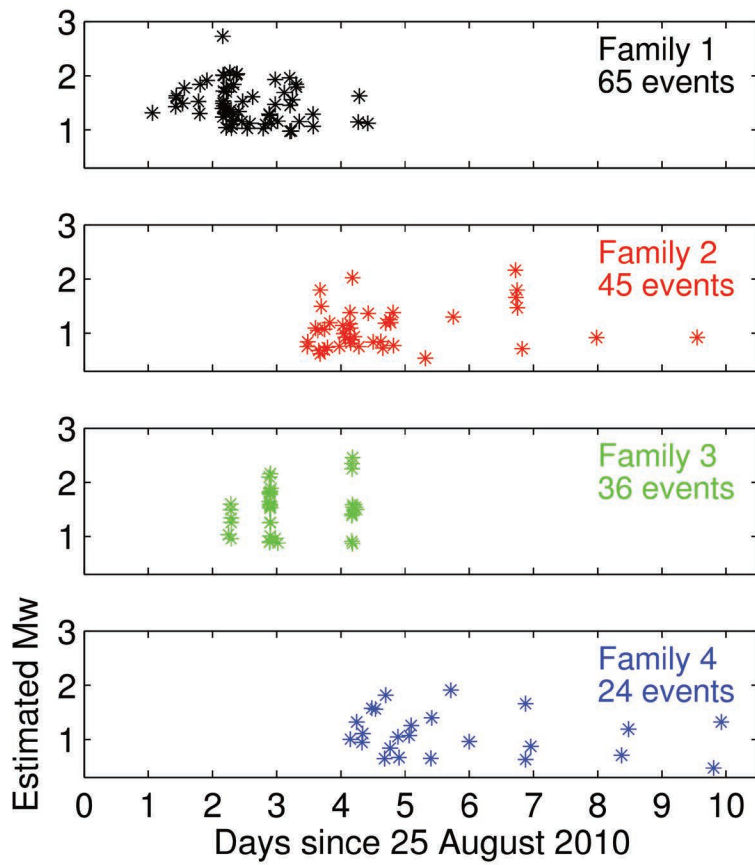


658

659

660 *Figure 15: Family character of the located seismicity. The circle diameters are scaled to the*
 661 *number of events similar to the located earthquake. The four largest families (including*
 662 *respectively 65, 45, 36 and 24 events) are contoured with the same colors as in Figure 14,*
 663 *and give the scale to the family population. Black dots show individual events, and the*
 664 *smallest empty circles are doublets. The depth of the subduction interface is contoured and*
 665 *labeled (in km) as in Figure 3.*

666



667

668

669 *Figure 16: Temporal activation of the 4 main seismicity families. The moment magnitude*
 670 *(Mw, vertical scale) has been derived using the amplitude ratio between each event and the*
 671 *larger event of the family, for which we have an independent estimate of the magnitude (see*
 672 *section 4.2)*

673

674

675

676

677

678

679

680 **5) Discussion and conclusions**

681

682 **5.1) SSE scaling laws**

683

684 The increasing number of SSEs observed in several subduction zones has offered the
685 possibility to examine their scaling relations (*Ide et al.*, 2007; *Peng and Gomberg*, 2010; *Gao*
686 *et al.*, 2012). These studies have enlightened the fact that the moment released during SSEs
687 appears to be proportional to their duration, which differs from the earthquakes behavior
688 where seismic moment grows as the cube of the duration. In this respect, the Central Ecuador
689 SSE ($M_w=6.0-6.3$ associated with a duration of 6-7 days) is well aligned with the trend
690 observed by *Ide et al.* (2007).

691

692 On the other hand, the slip extension appears to be more compact than for the other
693 documented SSEs. This characteristic is directly related to static stress drop, that can be
694 estimated from any coseismic slip distribution using the formalism of *Sato* (1972) (see also
695 *Singh* (1977)). When using the Gaussian model of equation (3), together with a characteristic
696 dimension R of the SSE, average stress drop can therefore be determined. We use a value for
697 R equal to $1.25D$ (D is defined in equation (3)). In this case, 79% of the moment is included
698 inside the disc of radius R . Considering the extreme values for D (6km-13km) and s_{max} (10cm-
699 40cm) determined in section 3, we find that stress drop is in the range 0.07-0.7MPa. These
700 values are not abnormal for earthquakes, but are significantly larger than the ones observed
701 for SSEs, which are typically of the order of 0.0001-0.01MPa (*Gao et al.*, 2012). This
702 suggests that some classes of SSEs may share some of the characteristics of earthquakes,
703 which differs from the conclusions of *Ide et al.* (2007). As a matter of fact, these authors
704 propose that slow and rapid processes have completely distinct behaviors. Our observation

705 rather supports a larger diversity in the scaling laws of the deformation processes, in better
706 agreement with the study of *Peng and Gomberg (2010)*.

707

708 **5.2) Relations between slow slip and seismicity**

709

710 This study provides some striking evidence of the seismic triggering potential of slow
711 slip processes. This causality has been observed in other subduction zones (Hikurangi, New
712 Zealand; Boso Peninsula, Japan; Guerrero, Mexico), but with less accuracy on the spatio-
713 temporal properties relating the two phenomena. It has also been suggested based only on
714 abnormal characteristics of the seismicity (*Holtkamp and Brudzinski, 2011; Holtkamp et al.,*
715 *2011; Kato et al., 2012; Bouchon et al., 2011*). Our study strongly supports that a peculiar
716 behavior of the seismicity, expressed by swarms or repeated events, may find its origin in a
717 slow slip process.

718

719 Figure 17 shows the spatial distribution of the slow slip and of its associated
720 seismicity. It reveals that most of the seismicity occurred inside or very close to the zone
721 affected by the slow slip. In other words, the spatial extension of the seismic crisis is a good
722 first-order evaluation of the size and location of the SSE. This was not the case for seismicity
723 associated to other SSEs (Hikurangi, New Zealand, *Delahaye et al., 2009*; Boso, Japan,
724 *Sagiya, 2004*; Guerrero, Mexico, *Liu et al., 2007*), where the earthquakes were adjacent to the
725 slow slip area. In particular, slow slip and seismicity are both shown to be active below La
726 Plata Island: we have shown in Figure 6 that slow slip is required below the Island, and our
727 location technique is especially robust for vertically propagating rays, as the velocity structure
728 effects are reduced. Two interpretations may account for this observation. This can be
729 explained by a mostly aseismic subduction interface, but over which small and localized

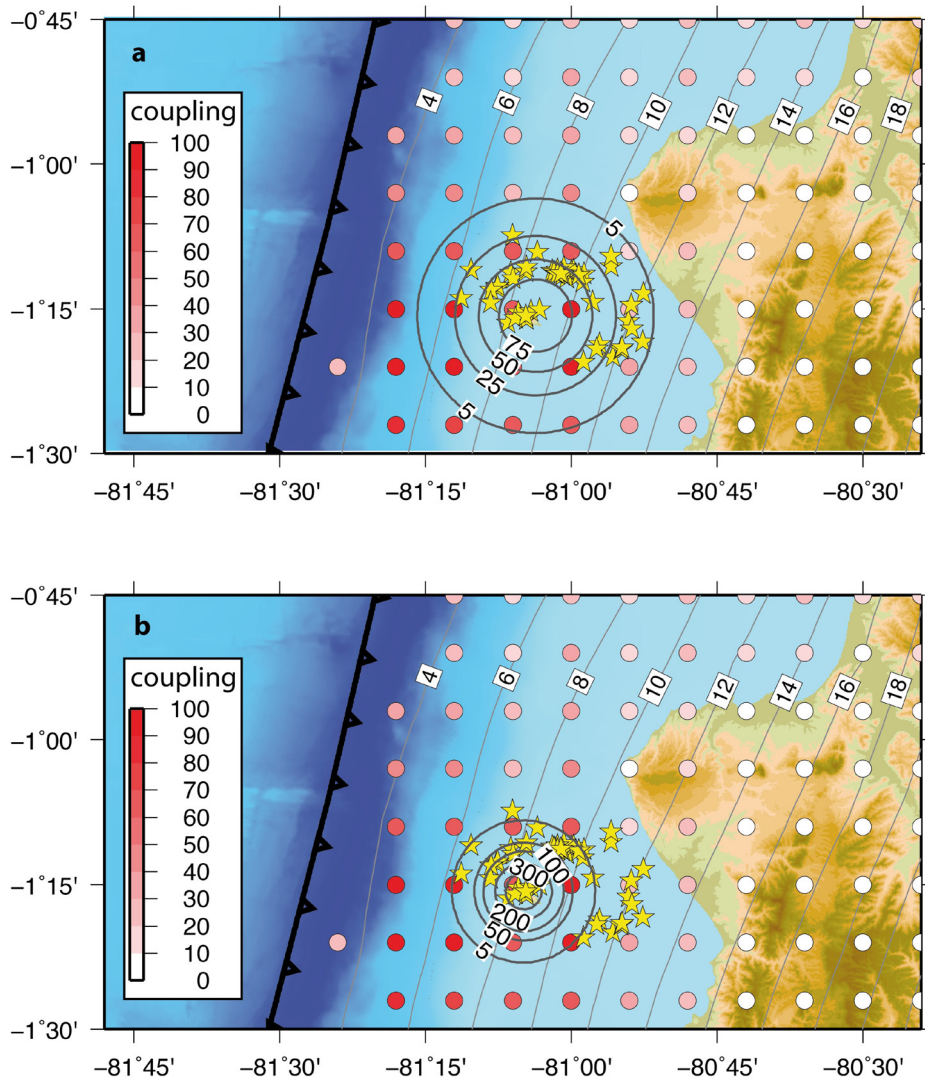
730 patches break seismically. However, since earthquakes have a magnitude lower than ~4, most
731 of them accommodate a displacement well below the centimeter level, if we assume classical
732 seismic scaling laws to be valid. Thus, the seismic slip for a given patch should still be small
733 compared to its full motion during the SSE. This -in turn- implies that the seismic patches
734 should have themselves a mixed behavior, partitioned between seismic and aseismic
735 processes, to be consistent with several centimeters of slip on the plate interface.
736 Alternatively, the seismicity may have occurred on small structures, surrounding the main
737 subduction interface where the slow slip developed. Small faults connected to the interface,
738 directly above or below it, would be candidates for this associated seismicity.

739

740 Both interpretations imply that seismicity is intimately related to the slow slip process.
741 This offers a way to derive some spatio-temporal characteristics of the SSE by tracking the
742 characteristics of the seismicity. In particular, rupture velocity of the SSE can be evaluated by
743 the location and occurrence time of the earthquakes. When looking at the 49 located
744 earthquakes, propagation from Northeast to Southwest is visible; however, this tendency
745 shows a large scatter, probably because, at a given location, earthquakes may occur some
746 hours or days after the activation of the slow slip (as shown by the temporal distribution of the
747 main families, Figure 16). Therefore rupture velocity can be better determined by the location
748 and activation initiation of families of repeating earthquakes rather than by the temporal
749 evolution of seismicity itself. Using this hypothesis for the four main families, we evaluate the
750 rupture velocity of the SSE to 5-7km/day. This value is consistent with other slow slip
751 processes compiled by *Gao et al.* (2012).

752

753



754

755

756 *Figure 17: Map view of the slow slip models as in Figure 7 together with the observed*
 757 *seismicity during the SSE. Epicenters are shown by yellow stars. Numbers along the*
 758 *concentric circles indicate isovalues of slip (in mm) as in Figure 7. Depth contours of the*
 759 *subduction interface and coupling spatial distribution are indicated as in Figure 3 and 7. In*
 760 *the case a), which corresponds to the upper bound of the slow slip spatial extend, all the*
 761 *seismicity is located inside the slow slip area. In the case b), which corresponds to the lower*
 762 *bound of the slow slip area, only the easternmost events are located outside the slow slip*
 763 *area.*

764 This well-documented case may be used as a typical example when simulating,
765 numerically or analogically, the coexistence of slow and rapid deformation processes. We
766 show that the slow slip event has activated seismicity that represents no more than a few
767 tenths of percent of the global deformation (in terms of released moment). Moreover, we
768 show that this seismicity is not homogeneously distributed in space and time. Some localized
769 zones are the loci of an intense seismic activity, as evidenced by the families of repeating
770 earthquakes. These elements may be compared with laboratory experiments, as the one of
771 *Lengliné et al.* (2012). Reciprocally, if experiments are able to reproduce these observed
772 properties, we should gain information on the frictional characteristics of the subduction
773 interface.

774

775 **5.3) Seismic cycle and SSEs in Central Ecuador**

776

777 Along the subduction segment in the vicinity of the La Plata Island, the coexistence of
778 slow slip processes and seismicity has likely already occurred repeatedly in the past. Since the
779 installation of station ISPT at the end of 2008, geodetic measurements have not revealed any
780 other clear transient signal. Before this date, seismicity remains the best indicator of
781 occurrence of similar episode of deformation. In this respect, the 3 swarms of 1998, 2002 and
782 2005 are obvious candidates (Figure 2). If referring to their larger spatial extension, to their
783 longer duration (month(s) instead of one week), and to their larger cumulated seismic moment
784 ($M_w \sim 6.5$ for the 2005 swarm, compared to $M_w \sim 4.2$ for the 2010 swarm), we suggest that
785 this seismicity originated from larger scale SSEs. The SSE potentially related to the strong
786 2005 swarm has not been detected by the INSAR analysis of *Holtkamp et al.* (2011), but as
787 explained by these authors, this is mainly due to the loss of coherence of satellite images.

788

789 Frequent SSEs should reduce the size and/or postpone the occurrence of an earthquake
790 breaking the coupled patch below La Plata Island (Figure 3). Seismic swarms thus appear to
791 be a detectable part of larger scale phenomena, which in turn play a significant role in the
792 seismic cycle. Their detection should then be a specific goal of seismic networks. While this
793 detection is sometimes possible at teleseismic distances, local networks are required for an
794 exhaustive analysis. In the specific case of Central Ecuador, future swarm activity should be
795 better monitored, as 5 offshore (OBS) seismometers have been deployed close to the trench
796 and associated with 6 on land seismometers installed on the Manta promontory.

797

798

799 **Acknowledgments**

800

801 We are grateful to the IRD (Institut de Recherche pour le Développement), ANR (Agence
802 Nationale de la Recherche, contract number ANR-07-BLAN-0143-01) and the IG-EPN for
803 strong support to the project of instrumentation of the Ecuadorian coast (“ADN” project). On
804 the Ecuadorian side, support was available from the Secretaría Nacional de Educación
805 Superior, Ciencia y Tecnología SENESCYT (Proyecto PIN_08-EPNGEO-00001). The
806 installation and maintenance of the seismic and geodetic arrays would not have been possible
807 without the help of numerous colleagues of the IG-EPN. This study also benefits from the
808 local seismicity catalog of the IG-EPN (RENSIG catalog). We thank F.Hirose and an
809 anonymous reviewer for their constructive comments which helped us to improve the initial
810 manuscript. The careful reading of the associate editor was also helpful. Some figures of this
811 article have been drawn using the GMT software (<http://gmt.soest.hawaii.edu/>).

812

813

814 **REFERENCES :**

815

816

817 Alessandrini, B., M. Cattaneo, M. Demartin, M. Gasperini, and V. Lanza (1994), A simple P-wave
818 polarization analysis: Its application to earthquake location, *Ann. Geophys.* 5, 883-897.

819

820 Andrews, D. J., and E. Schwerer (2000), Probability of rupture of multiple fault segments, *Bull.*
821 *Seismol. Soc. Am.*, 90, 1498-1506.

822

823 Beck, S., and L. Ruff (1984), The rupture process of the great 1979 Colombia earthquake: evidence
824 from the asperity model, *J. Geophys. Res.*, 89, 9281-9291.

825

826 Bejar-Pizarro, M., D. Carrizo, A. Socquet, R. Armijo, S. Barrientos, F. Bondoux, S. Bonvalot, J.
827 Campos, D. Comte, J. B. de Chabalier, O. Charade, A. Delorme, G. Gabalda, J. Galetzka, J. Genrich,
828 A. Necessian, M. Olcay, F. Ortega, I. Ortega, D. Remy, J. C. Ruegg, M. Simons, C. Valderas, and C.
829 Vigny (2010), Asperities and barriers on the seismogenic zone in North Chile: state-of-the-art after the
830 2007 Mw 7.7 Tocopilla earthquake inferred by GPS and InSAR data, *Geophys. J. Int.*, doi:
831 10.1111/j.1365-246X.2010.04748.x.

832

833 Béthoux, N., M. Segovia M., V. Alvarez, J.Y. Collot, P. Charvis, A. Gailler, and T. Monfret (2011),
834 Seismological study of the central Ecuadorian margin: Evidence of upper plate deformation, *Journal*
835 *of South American Earth Sciences*, 31, 139-152.

836

837 Bilek, S. L. (2010), Seismicity along the South American subduction zone: Review of large
838 earthquakes, tsunamis, and subduction zone complexity, *Tectonophysics*, 495, 2-14.

839

840 Bouchon, M. (1981), A simple method to calculate Green's functions for elastic layered media, *Bull.*
841 *Seism. Soc. Am.*, 71, 959-971.

842

843 Bouchon, M., H. Karabulut, M. Aktar, S. Özalaybey, J. Schmittbuhl, and M.P. Bouin (2011),
844 Extended Nucleation of the 1999 M-w 7.6 Izmit Earthquake, *Science*, 331, 877-880.

845

846 Chlieh, M., J. P. Avouac, K. Sieh, D. H. Natawidjaja, and J. Galetzka (2008), Heterogeneous coupling
847 of the Sumatran megathrust constrained by geodetic and paleogeodetic measurements, *J. Geophys.*
848 *Res.*, 113, B05305, doi:10.1029/2007JB004981.

849

850 Chlieh, M., H. Perfettini, H. Tavera, J.-P. Avouac, D. Remy, J.-M. Nocquet, F. Rolandone, F.
851 Bondoux, G. Gabalda, and S. Bonvalot (2011), Interseismic coupling and seismic potential along the
852 Central Andes subduction zone, *J. Geophys. Res.*, 116, B12405, doi:10.1029/2010JB008166.

853

854 Cohen, S.C. (1999), Numerical Models of Crustal Deformation in Seismic Zones, *Adv. Geophys.*, 41,
855 133-231.

856

857 Delahaye, E.J., J. Townend, M.E. Reyners, and G. Rogers (2009), Microseismicity but no tremor
858 accompanying slow slip in the Hikurangi subduction zone, New Zealand, *Earth Planet. Sci. Lett.*, 277,
859 21-28.

860

861 Dorbath, L., A. Cisternas, and C. Dorbath (1990), Assessment of the size of large and great historical
862 earthquakes in Peru, *Bull. Seismol. Soc. Am.*, 80, 551-576.

863

864 Douglas, A., J. Beavan, L. Wallace, and J. Townend (2005), Slow slip on the northern Hikurangi
865 subduction interface, New Zealand, *Geophys. Res. Lett.*, 32, L16305.

866

867 Dragert, H., K. Wang, and T. S. James (2001), A silent slip event on the deeper Cascadia subduction
868 interface, *Science*, 292, 1525-1528.

869

870 G. Ekström, M. Nettles, and A. M. Dziewonski (2012), The global CMT project 2004–2010: Centroid-
871 moment tensors for 13,017 earthquakes, *Phys. Earth Planet. Inter.*, 200–201, 1-9.

872

873 Engdahl, E. R., R. van der Hilst, and R. Buland (1998), Global teleseismic earthquake relocation with
874 improved travel times and procedures for depth determination, *Bull. Seism. Soc. Am.*, 88, 722-743.

875

876 Engdahl, E. R., and A. Villaseñor (2002), Global seismicity : 1900-1999, *International Handbook of*
877 *earthquake and engineering seismology*, 81A, 665-689.

878

879 Font, Y., H. Kao, S. Lallemand, C.-S. Liu, and L.-Y. Chiao (2004), Hypocentre determination offshore
880 of eastern Taiwan using the maximum intersection method, *Geophys. J. Int.*, 158, 655-675.

881

882 Font, Y., M. Segovia, S. Vaca and T. Theunissen (2013), Seismicity pattern along the Ecuadorian
883 subduction zone : New constrains from earthquake location in a 3D a priori velocity model, *Geophys.*
884 *J. Int.*, doi: 10.1093/gji/ggs083.

885

886 Freund, L.B., and D.M. Barnett (1976), A two dimensional analysis of surface deformation due to dip-
887 slip faulting, *Bull. Seismol. Soc. Am.*, 66, 667-675.

888

889 Gao, H., D. A. Schmidt, and R. Weldon (2012), Scaling relationships of source parameters for slow
890 slip events, *Bull. Seis. Soc. Am.*, 102, 352-360.

891

892 Graindorge, D., A. Calahorrano, P. Charvis, J.-Y. Collot, and N. Béthoux (2004), Deep structures of
893 the Ecuador convergent margin and the Carnegie Ridge, possible consequence on great earthquakes
894 recurrence interval, *Geophys. Res. Lett.*, *31*, L04603.

895

896 Gutscher, M. A., J. Malavieille, S. Lallemand, and J. Y. Collot (1999), Tectonic segmentation of the
897 North Andean margin: Impact of the Carnegie Ridge collision, *Earth Planet. Sci. Lett.*, *168*, 255–270.

898

899 Hirose, H., K. Hirahara, F. Kimata, N. Fujii, and S. Miyazaki (1999), A slow thrust slip event
900 following the two 1996 Hyuganada earthquakes beneath the Bungo Channel, southwest Japan,
901 *Geophys. Res. Lett.*, *26*, 3237-3240.

902

903 Holtkamp, S. G., and M.R. Brudzinski (2011), Earthquake swarms in circum-Pacific subduction
904 zones, *Earth Planet. Sci. Lett.*, *305*, 215-225, doi: 10.1016/j.epsl.2011.03.004,.

905

906 Holtkamp, S.G., M.E. Pritchard, and R.B. Lohman (2011), Earthquake Swarms in South America,
907 *Geophys. J. Int.*, *187*, 128-146.

908

909 Ide, S., G.C. Beroza, D.R. Shelly, and T. Uchide (2007), A scaling law for slow earthquakes, *Nature*,
910 *447*, 76-79.

911

912 Kanamori, H., and K.C. McNally (1982), Variable rupture mode of the subduction zone along the
913 Ecuador-Colombia coast, *Bull. Seismol. Soc. Am.*, *72*, 1241-1253.

914

915 Kanda, R.V.S., and M. Simons (2010), An elastic plate model for interseismic deformation in
916 subduction zones, *J. Geophys. Res.*, *115*, B03405.

917

918 Kato, A., K. Obara, T. Igarashi, H. Tsuruoka, S. Nakagawa, and N. Hirata (2012), Propagation of slow
919 slip leading up to the 2011 M_w 9.0 Tohoku-Oki earthquake, *Science*, *33*, 705-708.

918 Kelleher, J. (1972), Rupture zones of large South American earthquakes and some predictions, *J.*
919 *Geophys. Res.*, 77, 2087-2097.

920 Kim, M.J., S.Y. Schwartz, and S. Bannister (2011), Non-volcanic tremor associated with the March
921 2010 Gisborne slow slip event at the Hikurangi subduction margin, New Zealand, *Geophys. Res. Lett.*,
922 38, L14301.

923

924 Lengliné, O., J.E. Elkhoury, G. Daniel, J. Schmittbuhl, R. Toussaint, J.-P. Ampuero, and M. Bouchon
925 (2012), Interplay of seismic and aseismic deformations during earthquake swarms: an experimental
926 approach, *Earth Plan. Sci. Lett.*, 331-332, 215-223.

927

928 Liu, Y., J.R. Rice, and K.M. Larson (2007), Seismicity variations associated with aseismic transients
929 in Guerrero, Mexico, 1995-2006, *Earth Planet. Sci. Lett.* 262, 493-504.

930

931 Manchuel, K., M. Régnier, N. Béthoux, Y. Font, V. Sallares, J. Diaz, and H. Yepes (2011). New
932 insights on the interseismic active deformation along the North Ecuadorian-South Colombian (NESC)
933 margin, *Tectonics*, 30, TC4003.

934

935 Mazzotti, S., and J. Adams (2004), Variability of near-term probability for the next great earthquake
936 on the Cascadia subduction zone, *Bull. Seismol. Soc. Am.* 94, 1954-1959.

937

938 McCaffrey, R., L.M. Wallace, and J. Beavan (2008), Slow slip and frictional transition at low
939 temperature at the Hikurangi subduction zone, *Nature Geoscience*, 1, 316-320.

940

941 Mendoza, C., and J. Dewey (1984), Seismicity associated with the great Colombia-Ecuador
942 earthquakes of 1942, 1958 and 1979: Implications for barrier models of earthquake rupture, *Bull.*
943 *Seismol. Soc. Am.*, 74, 577-593.

944

945 Métois, M., A. Socquet, and C. Vigny (2012), Interseismic coupling, segmentation and mechanical
946 behavior of the central Chile subduction zone, *J. Geophys. Res.*, *117*, B03406,
947 doi:10.1029/2011JB008736.

948

949 Moreno, M., M. Rosenau, and O. Oncken (2010), 2010 Maule earthquake slip correlates with pre-
950 seismic locking of Andean subduction zone, *Nature*, *467*, 198–202, doi:10.1038/nature09349.

951

952 Outerbridge, K. C., T. H. Dixon, S. Y. Schwartz, J. I. Walter, M. Protti, V. Gonzalez, J. Biggs, M.
953 Thorwart, and W. Rabbel (2010), A tremor and slip event on the Cocos-Caribbean subduction zone as
954 measured by a global positioning system (GPS) and seismic network on the Nicoya Peninsula, Costa
955 Rica, *J. Geophys. Res.*, *115*, B10408.

956

957 Ozawa, S., S. Miyazaki, Y. Hatanaka, T. Imakiire, M. Kaidzu, and M. Murakami (2003),
958 Characteristic silent earthquakes in the eastern part of the Boso peninsula, Central Japan, *Geophys.*
959 *Res. Lett.*, *30*, 1283.

960

961 Payero, J., V. Kostoglodov, N. Shapiro, T. Mikumo, A. Iglesias, X. Pérez-Campos, and R. Clayton
962 (2008), Nonvolcanic tremor observed in the Mexican subduction zone, *Geophys. Res. Lett.*, *35*,
963 L07305.

964

965 Peng, Z., and J. Gomberg (2010), An integrated perspective of the continuum between earthquakes
966 and slow-slip phenomena, *Nature Geoscience*, *3*, 599-607.

967

968 Pennington, W.D. (1981), Subduction of the Eastern Panama Basin and Seismotectonics of
969 Northwestern South America, *J. Geophys. Res.*, *86*, 10,753–10,770.

970

971 Radiguet, M., F. Cotton, M. Vergnolle, M. Campillo, B. Valette, V. Kostoglodov, and N. Cotte (2011),
972 Spatial and temporal evolution of a long term slow slip event: the 2006 Guerrero Slow Slip Event,
973 *Geophys. J. Int.*, 184, 816-828.
974

975 Rani, S., and S.J. Singh (1992), Static deformation of a uniform half-space due to a long dip-slip fault,
976 *Geophys. J. Int.*, 109, 469-476.
977

978 Rogers, G., and H. Dragert (2003), Episodic tremor and slip on the Cascadia subduction zone: The
979 chatter of silent slip, *Science*, 300, 1942-1943.
980

981 Ruegg, J. C., A. Rudloff, C. Vigny, R. Madariaga, J. B. de Chabalier, J. Campos, E. Kausel, S.
982 Barrientos, and D. Dimitrov (2009), Interseismic strain accumulation measured by GPS in the seismic
983 gap between Constitucion and Concepcion in Chile, *Phys. Earth Planet. In.*, 175, 78-85, doi:
984 10.1016/j.pepi.2008.02.015.
985

986 Sagiya, T. (2004), Interplate coupling in the Kanto district, central Japan, and the Boso Peninsula
987 silent earthquake in May 1996, *Pure Appl. Geophys.*, 161, 2601-2616.
988

989 Sato, R. (1972), Stress drop for a finite fault, *J. Phys. Earth*, 20, 397-407.
990

991 Savage, J.C. (1983), A dislocation model of strain accumulation and release at a subduction zone, *J.*
992 *Geophys. Res.*, 88, 4984-4996.
993

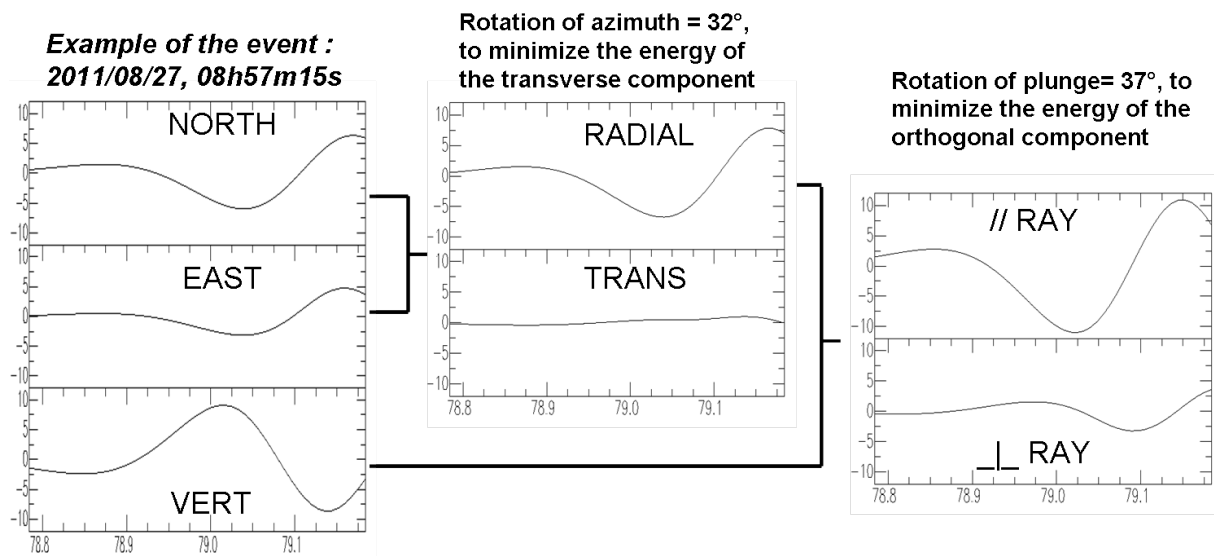
994 Schwartz, S.Y., and J.M. Rokosky (2007), Slow slip events and seismic tremor at circum-pacific
995 subduction zones, *Rev. Geophys.*, 45, RG3004.
996

997 Segovia, M. (2001), El sismo de Bahía del 4 de agosto de 1998: Caracterización del mecanismo de
998 ruptura y análisis de la sismicidad en la zona costera, *Tesis de previa a la obtención del título de*
999 *Ingeniera Geóloga thesis*, 126 pp, Escuela Politécnica Nacional, Quito, Ecuador (in Spanish).
1000
1001 Segovia, M., (2009), Análisis espacio-temporal del Enjambre de Puerto López entre enero y febrero de
1002 2005 con observaciones de la estación de banda ancha de OTAVALO, *Master thesis of University of*
1003 *Nice Sophia Antipolis*, Quito, Ecuador (in Spanish).
1004
1005 Singh, S.K. (1977), Slip and stress drop on a circular fault, *Bull. Seismol. Soc. Am.*, 67, 279-284.
1006
1007 Swenson, J. L., and S. L. Beck (1996), Historical 1942 Ecuador and 1942 Peru subduction
1008 earthquakes, and earthquake cycle along Colombia-Ecuador and Peru subduction segments, *Pure*
1009 *Appl. Geophys.*, 146, 67-101.
1010
1011 Tarantola, A. (2005), Inverse problem theory and methods for model parameter estimation, *Society for*
1012 *Industrial and Applied Mathematics (SIAM)*, Philadelphia.
1013
1014 Theunissen, T., Font, Y., Lallemand, S., and S. Gautier (2012), Improvements of the Maximum
1015 Intersection Method for 3D absolute earthquake location, *Bull. Seismol. Soc. Am.*, 102, 1764-1785.
1016
1017 Tomar, S., and N.K. Dhiman (2003), 2-D Deformation Analysis of a Half-space due to a Long Dip-
1018 slip Fault at Finite Depth, *Journal of Earth System Science*, 112, 587-596.
1019
1020 Trenkamp, R., J.N. Kellogg, J.T. Freymueller, and P. Mora (2002), Wide plate margin deformation,
1021 southern Central America and northwestern South America, CASA GPS observations, *Journal of*
1022 *South American Earth Sciences*, 15, 157-171.
1023

1024 Vaca, S., M. Regnier, N. Béthoux, V. Alvarez, and B. Pontoise (2009), Sismicidad de la región de
1025 Manta (Ecuador): enjambre sísmico de Manta-2005, *Geología y Geofísica Marina y Terrestre del*
1026 *Ecuador, Spec. Pub. INOCAR-IRD*, 151-166 (in spanish with english abstract).
1027
1028 Vidale, J. E., A. J. Hotovec, A. Ghosh, K. C. Creager, and J. Gomberg (2011), Tiny intraplate
1029 earthquakes triggered by nearby episodic tremor and slip in Cascadia, *Geochem. Geophys. Geosyst.*,
1030 *12*, Q06005.
1031
1032 Wallace, L. M., and J. Beavan (2010), Diverse slow slip behavior at the Hikurangi subduction margin,
1033 New Zealand, *J. Geophys. Res.*, *115*, B12402.
1034
1035 Wdowinski, S., Y. Bock, J. Zhang, P. Fang, and J. Genrich (1997), Southern California permanent
1036 GPS geodetic array: spatial filtering of daily positions for estimating coseismic and postseismic
1037 displacements induced by the 1992 Landers earthquake, *J. Geophys. Res.*, *102*, 18,057–18,070.
1038
1039 White, S.M., R. Trenkamp, and J. Kellogg (2003), Recent crustal deformation and the earthquake
1040 cycle along the Ecuador-Colombia subduction zone, *Earth Planet. Sci. Lett.*, *216*, 231-242.
1041
1042
1043
1044
1045
1046
1047
1048
1049
1050

1051 **Supplementary material :**

First 0.4s of the P waves, filtered in the range [1-4 Hz] (velocity)



1052
1053 *Supplementary Figure A.1 : Procedure used to determine the earthquakes location. (Left of the figure) :*
1054 *The three components are band-passed (1-4Hz) and windowed (0.4s) after the P wave arrival. (Middle)*
1055 *Search for the rotation angle (R_α) of the horizontal components minimizing the average squared*
1056 *amplitude on the initial East component. The back-azimuth of the earthquake is equal to R_α when the*
1057 *initial North component is anticorrelated with the vertical component. It is equal to $(R_\alpha + 180^\circ)$ in the*
1058 *case of positive correlation. The back-azimuth is here found equal to 32° . (Right of the figure) Same*
1059 *operation with the radial and vertical component to determine the optimal apparent incident angle of*
1060 *the ray, here found equal to 37° . Note that this angle is apparent because it is not the real incidence*
1061 *angle due to free surface effects (see Aki and Richards, 2002). Relative amplitude between the vertical*
1062 *and radial components imply that the measured angle is $(2j)$, where j is the angle of the reflected S-*
1063 *wave corresponding to the real P-wave incidence i . Simple application of the Snell-Descartes law*
1064 *allows us to retrieve i from $(2j)$. This relation between $2j$ and i is not dependent on the absolute value of*
1065 *the wave velocities, but only on the ratio between P-velocity and S-velocity, here taken equal to $\sqrt{3}$.*
1066 *Using this relation, $i=33.4^\circ$. From the value of i , the ray geometry is predicted using the two-layer*
1067 *model of table 1, and the hypocenter position along this ray is determined by the S-P time.*

1068 **Supplementary material references :**

1069 Aki, K., and P. Richards (2002), Quantitative Seismology, Univ. Sci., Sausalito, Calif.